



Polymer-based laminar probes with an ultra-long flexible spiral-shaped cable for in vivo neural recordings

Csaba Horváth^{a,b,1}, Klaudia Csikós^{a,b,1}, Borbála Árkossy^c, Eric Klein^{d,e}, Patrick Ruther^{d,e}, István Ulbert^{a,c,*}, Richárd Fiáth^{a,c}

^a Institute of Cognitive Neuroscience and Psychology, HUN-REN Research Centre for Natural Sciences, Budapest 1117, Hungary

^b János Szentágothai Doctoral School of Neurosciences, Semmelweis University, Budapest 1083, Hungary

^c Faculty of Information Technology and Bionics, Pázmány Péter Catholic University, Budapest 1083, Hungary

^d Department of Microsystems Engineering (IMTEK), University of Freiburg, Freiburg 79108, Germany

^e University Center BrainLinks-BrainTools, University of Freiburg, Freiburg 79110, Germany

ARTICLE INFO

Keywords:

Neural implant
Flexible probe
Polyimide
Microelectrode
In vivo neural recording
Single unit activity

ABSTRACT

Compared to conventional rigid silicon probes, flexible penetrating neural implants exhibit improved mechanical compliance with brain tissue, enabling high-quality neural recordings over extended periods of time. However, the length of the implantable shank and extension cable of most flexible devices falls short of clinical electrodes used in diagnostics and treatment of neurological disorders. In this study, we demonstrate the design, fabrication, and in vivo validation of polyimide-based neural probes with a thin spiral-shaped cable that reaches a length of 27 centimeters, comparable to that of clinical electrodes. The spiral probe comprises a 3.9-mm-long, 75–280-μm-wide and 10-μm-thick implantable shank with 24 linearly placed gold microelectrodes (diameter: 20 μm; electrode pitch: 150 μm) placed either close to the shank edge or centered on the shank. The electrical impedance of the microelectrodes was ~266 kΩ at 1 kHz measured in vitro. In acute rodent experiments, we recorded high-quality local field potentials (e.g., cortical slow waves and hippocampal gamma activity), single and multiunit activities. In addition, the probes could simultaneously detect the activity of about 10 well-isolated single units, with an average spike amplitude of 65 μV. Furthermore, devices chronically implanted in rats successfully recorded spiking activity over several consecutive days. As demonstrated here, the developed spiral probes can be applied to various tasks, such as the laminar analysis of brain oscillations or the study of the sleep-wake cycle in naturally sleeping animals. In conclusion, our flexible probe design may stimulate the development of novel implantable devices for application in large animal models or clinical settings.

1. Introduction

In basic neuroscience research and various clinical settings, implantable neural devices currently serve as the core tools for electrically recording and manipulating local brain activity at submillisecond resolution [1–4]. Among these tools, rigid silicon-based probes, fabricated using thin-film micro-electromechanical systems (MEMS) technologies, are the most widely applied invasive brain implants for research purposes [5–9]. While silicon probes provide high-fidelity electrophysiological recordings in acute settings from anesthetized and head-fixed animals, their recording performance typically deteriorates within a few weeks or months, when chronically implanted in freely

moving or behaving animals [10–12].

One of the main causes behind this decline in performance is the mechanical mismatch between the stiff probe shanks and the much softer brain tissue. While silicon has an elastic (Young's) modulus of ~170 GPa, the Young's modulus of brain tissue is many orders of magnitude lower, approximately 0.1 – 6 kPa [13]. This difference in flexibility has been shown to have several adverse implications for long-term in vivo neural recordings. For instance, in acute rat experiments, continuous micromotion of the brain tissue relative to the rigid probe (or vice versa) was observed due to factors such as breathing, vascular pulsations or head displacements [14]. These micromotions, with amplitudes in the range of several micrometers, generate a constant

* Corresponding author at: Institute of Cognitive Neuroscience and Psychology, HUN-REN Research Centre for Natural Sciences, Budapest 1117, Hungary.

E-mail address: ulbert.istvan@ttk.hu (I. Ulbert).

¹ These authors contributed equally.

friction between the brain and the implanted probe shank, presumably aggravating the foreign body response in the tissue adjacent to the implant. For this, as well as for other reasons, long-term probe implantations typically lead to the formation of a thick glial sheath around the probe shank, effectively sealing the monitored/stimulated neurons from the microelectrodes [10,15,16]. Additionally, substantial neuronal damage, cell loss, and inflammation are commonly observed in the immediate proximity of chronically implanted rigid devices [15–18]. Experimental evidence suggests that the severity of this tissue response is also influenced by the dimensions of the implanted device (e.g., the cross-sectional area of the probe shanks), with larger devices inflicting more damage to the tissue [19].

The findings of above studies also have implications for brain implants used in clinical settings. Conventional rigid stereo-electroencephalography (SEEG) and deep brain stimulation (DBS) probes, employed for the diagnosis or treatment of human neurological disorders (e.g., epilepsy, Parkinson's disease, or essential tremor), comprise an implantable stiff cylindrical shank with a diameter ranging from 0.8 mm to 1.27 mm. This size translates to a cross-sectional area two orders of magnitude larger than that of the shanks of state-of-the-art silicon-based probes [2–4]. The substantial difference in the surgical footprint of these devices implies that the application of bulky clinical SEEG and DBS probes in human patients poses a considerable risk of causing severe neuronal damage and eliciting a strong tissue response along the insertion track of the neural probe. These adverse effects may significantly impair the diagnostic and stimulation performance of these devices, both in the short and long term. The consequence of these effects is even more critical if the activity of local neuron populations or individual neurons located close to the macro- and microelectrodes of the implant is considered.

To mitigate the tissue response to implanted neural interfaces, recent studies have focused on the development of more flexible neural probes fabricated from softer materials, such as polymeric substrates (e.g., polyimide, Parylene C, and SU-8; [20–29]). These soft materials have a closer match with the mechanical properties of the brain tissue. In addition, polymer-based probes can be readily manufactured by applying essentially the same micromachining processes that are used for the fabrication of silicon probes. These flexible probes achieve better compliance with the brain tissue and a reduced foreign body response, leading to prolonged recording of high-quality neural signals [24, 30–35]. However, the implantable shank of these devices, as well as the length of their cabling are typically limited to a few tens of millimeters, constrained by the size of the 4-inch silicon wafers (100 mm diameter) most commonly used for fabrication in this field. This limitation considerably restricts the use of these devices in larger (preclinical) animal models (e.g. non-human primates), or for clinical applications where lead lengths exceeding 20 centimeters are often required. Improving the dimensions of flexible implants presents an opportunity to initiate the development of a potentially new generation of human-applicable devices with a significantly reduced surgical footprint and improved mechanical compliance with the brain tissue compared to current bulkier devices. Longer flexible implants may also fuel research conducted in larger (preclinical) animal species, which in turn could also facilitate the faster translation of novel neurotechnologies and treatments for human use.

In this work, we demonstrate the design, fabrication and *in vivo* validation of a planar flexible neural probe featuring a spiral-shaped cable with a length close to that of clinical electrodes (~30 cm). The polyimide-based device, manufactured on 4-inch silicon wafers, comprises a thin implantable shank with 24 microelectrodes arranged equidistantly in a linear configuration along the long axis of the probe shank. The linear electrode layout was designed with the intention to study the neural activity of laminar brain structures, such as the neocortex or the hippocampus [36,37]. After functional characterization of our probes under *in vitro* conditions, we characterized their short-term recording performance in acute experiments through

implantations into the brain tissue of anesthetized rodents. To assess their long-term electrical functionality and recording performance, we chronically implanted probes in three rats for a period of two weeks. Evaluation of the recording quality of the probe was based on single unit numbers and spike amplitudes extracted from both acute and chronic electrophysiological recordings. In this study, we designed and realized two shank variants: one with microelectrodes located close to edge of the probe shank and another with electrodes positioned in the middle of the shank along its long axis. The acute recording performance of the two probe types was also compared. Finally, we constructed laminar depth profiles of measured cortical activity, and compared their qualitative properties to our findings obtained with laminar silicon probes [38].

2. Materials and methods

2.1. Probe design

The layout of the spiral probes is shown in Fig. 1A. Each spiral probe comprises a straight implantable probe shank hosting a linear micro-electrode array, a spiral-shaped probe cable, and a connector part. The electrode array consists of 24 gold microelectrodes with a diameter of 20 μm arranged at a pitch of 150 μm . The microelectrodes are either centered on the probe shank (center design) or positioned close to the probe shank edge (edge design), as illustrated in Fig. 1B. The spiral cable is composed of 3 half circles of increasing diameter such that 8 spiral probes fit onto the design space of a 4-inch silicon wafer, as illustrated in Fig. 1C. We have chosen a compromise between overall length and the minimal radius of a spiral half loop, as smaller radii tend to make straightening of the spiral more difficult. Our design approach was as follows. Spiral sections covering 90° had inner radii between 35.4 mm and 23.5 mm, changing in steps of 1 mm. This configuration allowed us to place the spiral quarter sections in such a way that a spacing of 500 μm remained between the spirals as shown in Fig. 1C. The cable of a single probe hosts 24 metal tracks, each with a line width and spacing of 10 μm . The connector part is designed to fit either a 36-channel Omnetics connector (36 Position Dual Row Male Nano-Miniature Connector; part number: A79022-001; Omnetics Connector Corporation, MN, United States) or a 25-channel zero insertion force (ZIF) connector with a pad pitch of 250 μm , as illustrated in Fig. 1A (inset). Additionally, each probe contains a small, slotted hole at the tip of the shank for insertion purposes (Fig. 1B). This feature was utilized in one of the chronic experiments, where the probe was successfully implanted into deep brain regions with the aid of a shuttle device.

2.2. Fabrication process

The probe fabrication is similar to established polyimide (PI) processes used to realize ribbon cables interconnecting silicon-based neural probes [39], cylindrically-shaped probes [40], optical implants [41] as well as flexible neural probes [42]. As illustrated in Fig. 1D(1), a first 5- μm -thick PI layer is spin-coated onto a 4-inch silicon wafer, which serves as the substrate material. The PI layer is then cured and subsequently activated using an oxygen plasma. Next, a 100-nm-thick platinum (Pt) layer is sputter deposited and patterned using a dual layer lift-off process applying LOR-5A (MicroChem, MA, United States) and AZ 1518 (Microchemicals, Ulm, Germany) photoresists, as described in [43] and shown in Fig. 1D(2). The Pt serves as an adhesion promoter to the underlying PI layer. Subsequently, a titanium (Ti)-gold (Au)-Ti layer stack with thicknesses of 50/150/50 nm is sputter deposited in a maskless manner. As a masking layer for the subsequent electroplating step, AZ 9260 (Microchemicals) with a thickness of 10 μm is deposited and patterned using photolithography. Prior to Au-electroplating applied to lower the electrical line resistance, the upper Ti layer is removed in 1 %-hydrofluoric acid (HF). The electroplating step thickens the metal tracks by 1 μm . After resist stripping using acetone, the seed

layer around the electroplated tracks is removed using 1 % HF, gold etch (potassium iodine (KI)) and 1 % HF to remove the Ti, Au and Ti layers (see in Fig. 1D(3)), respectively. Next, a second PI layer of 5 μm in thickness is spin coated and cured, as indicated in Fig. 1D(4). The contact pads on the probe base, the microelectrodes at the probe shank and the probe contour are defined by photolithography patterning AZ 9260 as a masking layer and reactive ion etching (RIE) to selectively structure the PI layer stack (see in Fig. 1D(5)). Next, contact pads and microelectrodes are gold-electroplated to a thickness of 7 μm , as indicated in Fig. 1D(6). Finally, the probes are peeled off the silicon substrate using tweezers.

2.3. Probe characterization

2.3.1. In vitro characterization

Electrical impedance spectroscopy of 360 microelectrodes of 15 probes was performed similarly as described in [44]. Briefly, impedance magnitude was measured using an Intan RHD-2000 electrophysiological recording system (Intan Technologies LLC, CA, United States). Measurements were performed in vitro in 0.9 % NaCl solution using an Ag/AgCl reference electrode at thirteen biologically relevant frequencies (ranging from 1 Hz to 7.5 kHz). Microelectrodes showing impedance values (measured at 1 kHz) above 1 M Ω (indicating putative open circuits) and below 50 k Ω (indicating putative short circuits) were excluded from further analysis ($n = 95$ electrodes; 26.4 %). In addition, we measured the series resistance of 15 metal tracks across four different probes (two probes with ZIF connectors and two probes with Omnetics connectors) using a digital multimeter. Finally, we computed the root mean square (RMS) noise level in the local field potential (1 – 500 Hz) and action potential (500 – 5000 Hz) frequency bands on in vitro recordings acquired with several microelectrodes ($n = 68$ electrodes of 3 probes) in saline solution.

2.3.2. In vivo measurements

Acute and chronic in vivo experiments followed the guidelines set by the EC Council Directive of September 22, 2010 (2010/63/EU) and received approval from both the Animal Care Committee of the Research Centre for Natural Sciences of the Hungarian Academy of Sciences and the National Food Chain Safety Office of Hungary (license number: PE/EA/775–7/2020). To characterize the developed probes, we collected neural recordings from anesthetized rodents. In these acute experiments adult Wistar rats ($n = 9$; weight: $320 \text{ g} \pm 95 \text{ g}$, mean \pm standard

deviation; 5 females) and adult C57BL/6 J mice ($n = 3$; weight: $24 \text{ g} \pm 4 \text{ g}$; 2 males) were used. Furthermore, probes were also chronically implanted in three adult Wistar rats (weight: 375 g, 441 g, and 236 g; two males).

2.3.2.1. Animal surgery and acute recordings in anesthetized rodents. For acute rodent experiments, we adopted methods used in our earlier studies [38,45]. In short, rats and mice were anesthetized by an intraperitoneal injection of ketamine (75 mg/kg body weight for rats and 100 mg/kg for mice) and xylazine (10 mg/kg body weight for both rats and mice). During surgery and neural recordings, additional doses of ketamine/xylazine mixture were administered regularly (1–2 intramuscular injections per hour) to maintain a stable deep anesthetic state. Animals were warmed from below using a homeothermic heating pad (Supertech, Pécs, Hungary). After securing the head of the rodents in a stereotaxic frame (David Kopf Instruments, Tujunga, CA, United States), we carefully removed the skin and periosteum to expose the dorsal part of the skull. Next, a square-shaped cranial window with a side length of 3 mm (2 mm in mice) was prepared over the left hemisphere using a dental drill. Typically, the craniotomy was centered 3 mm posterior (1.5 mm in mice) and 3 mm lateral (1.5 mm in mice) relative to the bregma, to expose the primary somatosensory and parietal association cortices [46,47]. To reduce the dimpling of the brain tissue during the insertion of our polymer-based flexible probes, the dura mater was carefully pierced over the target site using a fine (34 gauge) needle. In cases where the probe could not penetrate the brain tissue on the first attempt, small incisions were made in the pia mater using the same needle to aid the insertion.

Two different approaches were employed for acute probe insertion (Fig. S1). In the first insertion method ($n = 3$ insertions in 2 rats), we aligned the probe shank with the shank of a silicon-based dummy probe used as an insertion aid [48,49], and then affixed them together using a small amount of liquid polyethylene glycol (PEG 1500, MW 1500; Fig. S1A; [50]), a biocompatible hydrogel [51]. The attached probes were then inserted into the brain tissue. After a few minutes, when the PEG dissolved, the silicon probe was carefully retracted, leaving the flexible probe in the tissue. In the second insertion method ($n = 10$ insertions in 7 rats; $n = 5$ insertions in 3 mice), first, a small Sections (1–2 mm) of the PI cable right next to the top of the probe shank was attached to the end of a small 3D printed rectangle (1 mm \times 2 mm \times 30 mm; thickness \times width \times length) using a small droplet of liquid PEG 1500 (Fig. S1B). Care was taken to align the probe shank (~ 4 mm) parallel to

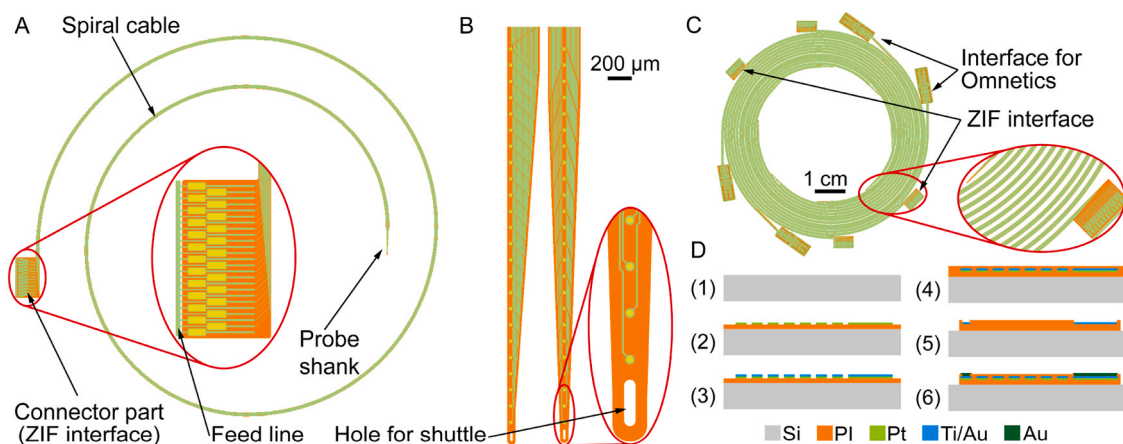


Fig. 1. Probe design and fabrication steps. (A) Layout of the spiral probe with zero insertion force (ZIF) interface shown in the inset, (B) probe shank variants with a slotted hole for shuttle insertion and microelectrodes positioned at the shank edge (left) or symmetrically in the shank center (right), (C) arrangement of eight spiral probes with interfaces to either a ZIF or Omnetics connector on a 4-inch processing wafer, and (D) main process steps (1) spin-coating of polyimide (PI), (2) deposition and patterning of Pt using sputtering and lift-off, (3) seed layer deposition, lithography, Au-electroplating and seed layer removal, (4) spin-coating of 2nd PI layer, (5) reactive ion etching of PI layer stacks to define microelectrode sites, contact pads and probe contour, and (6) Au-electroplating of microelectrodes and contact pads.

the long axis of the 3D printed component.

Next, either the dummy probe/flexible probe complex, or the 3D printed component with the attached flexible probe was secured to a motorized stereotaxic micromanipulator (Robot Stereotaxic, Neurostar, Tübingen, Germany). The probe shank was then slowly inserted into the brain tissue at rate of 100 $\mu\text{m}/\text{sec}$ for the insertion method with the silicon dummy probe, and 2 $\mu\text{m}/\text{sec}$ for the second insertion method. We visually tracked the advancement of the microelectrodes using a stereomicroscope. The probes were implanted to a depth of approximately 3.5 mm (range: 2.7 – 4 mm in rats; 3 – 3.9 mm in mice), with a few (2–5) electrodes typically located above the cortical surface. This depth allowed us to simultaneously record the activity of the neocortex and the hippocampus, including also the activity of dorsal nuclei of the thalamus in mice. The surface of the brain tissue was kept moist using room temperature physiological saline solution. As an external reference electrode, we applied a hypodermic needle placed above the neck muscle. The same electrode was also used for grounding.

Acute in vivo neural data was collected using an Intan RHD-2000 electrophysiological recording system [45]. A 32-channel headstage with an Omnetics connector was used to record from the 24 microelectrodes. For probes with a ZIF interface ($n = 6$ probes tested), the headstage was connected to a custom ZIF-to-Omnetics adapter printed circuit board (PCB; ATLAS Neuroengineering, Leuven, Belgium). The ZIF interface of the probe was directly attached to the ZIF connector of the adapter PCB. For probes with an Omnetics connector (soldered to the contact pads of the probe; $n = 1$ probe tested), the probe was connected directly to the headstage, without an adapter. The recording system acquired spontaneously occurring wideband signals (0.1 – 7500 Hz) with 16-bit resolution at a sampling rate of 20 kHz per channel. From a single brain location, about 30 minutes of neural data were collected (30.79 ± 18.22 min; range: 5 – 77 min). Typically, one or two flexible probes were implanted during an acute experiment, and 2–5 recordings were obtained from one or two different brain locations (penetrations). In a subset of experiments ($n = 7$ penetrations in 6 rats, $n = 2$ penetrations in 1 mouse), the probe was carefully detached from the 3D printed component by dissolving the PEG with saline solution. Neural activity was recorded both before and after detachment to compare the recording quality (Fig. S2). All collected data were saved to a network-attached storage device for further analysis. A total of 26 rat and 9 mouse recordings were obtained during the study (Table 1).

2.3.2.2. Chronic probe implantation procedure and recordings in freely moving rats. One edge type and two center type probes were implanted in separate animals. The applied chronic probe implantation procedure was adapted from our previously published study [45]. In short, rats were anesthetized with intraperitoneally injected ketamine/xylazine mixture, then secured in a stereotaxic frame. Physiological body temperature of the animals was maintained during surgical procedures until they woke up from anesthesia. Prior to surgery, a subcutaneous injection of 0.1 ml meloxicam (1 mg/kg; Dopharma Research, Raamsdonksveer, Netherlands) was administered to alleviate inflammation and pain. Using a scalpel, we made a small incision in the skin on the top of the head along the midline, then the skin was retracted with four pean forceps. Next, dental etching gel with 38 % phosphoric acid (Etch-Rite, PULPDENT Corporation, Watertown, MA, United States) was applied to the cleaned skull surface to improve the adhesion of dental cement used at a later stage of the surgery. Additionally, four bone screws, each with a diameter of 0.9 mm and length of 2 mm (ATLAS Neuroengineering)

were driven into the skull in a semi-circular pattern for stabilization purposes. As a reference and ground electrode, we used a 3 mm long bone screw with a diameter of 0.9 mm driven into the bone above the cerebellum. A $2 \times 2 \text{ mm}^2$ square-shaped cranial window was then drilled over the target brain region (primary somatosensory cortex and hippocampus, or the thalamus), centered 3.0 mm posterior and 3.0 mm lateral to the bregma. Sterile physiological saline solution was used to keep the brain surface moist. Furthermore, to prevent ocular dehydration, eye ointment (Corneregel, Dr. Gerhard Mann Chem.-Pharm. Fabrik GmbH, Germany) was frequently applied to the eyes of the animal. To facilitate probe insertion and decrease brain dimpling, the meninges were carefully removed over the insertion site using a sterile hypodermic needle (34 gauge). Next, in two rats, the flexible probe mounted on a motorized stereotaxic micromanipulator (affixed with PEG to a 3D printed component, as described in Section 2.3.2.1) was positioned over the insertion site and slowly (2 $\mu\text{m}/\text{s}$) implanted into the brain tissue to a depth of 3.2 mm from the cortical surface. After that, we sealed the exposed brain surface in the craniotomy with a soft, two-component silicone gel (DuraGel, Cambridge NeuroTech, Cambridge, United Kingdom). Once the DuraGel cured, the cranial window was covered with a thin layer of light-curable dental cement (RelyX Universal Resin Cement, 3 M, St. Paul, MN, United States). Finally, the probe was detached from the micromanipulator by dissolving the PEG with saline solution. For the third rat, we used a thin tungsten microelectrode (125 μm in diameter; FHC, Bowdoin, ME, United States) as a shuttle device. The shank of the flexible probe was laid on the surface of the cortex (parallel to cortical layers), with the tip of the probe positioned in the center of the craniotomy, over the target area. The sharp tip of the tungsten microelectrode was then carefully inserted from above into the small hole located at the tip of the flexible probe (Fig. 1B). Next, the tungsten electrode was moved to a depth of 8 mm (to target the thalamus) at an insertion speed of 0.1 mm/s, dragging the flexible probe into the brain tissue. Upon reaching the target depth, the tungsten electrode was retracted at the same speed, leaving the flexible probe at the implanted depth with minimal displacement. Finally, the craniotomy was covered with dental cement.

To protect the probe, the headstage and the adapter PCB from mechanical damage, as well as to facilitate the connection of the probe to the recording equipment during the recording sessions, we applied in our chronic experiments a slightly modified version of the 3D printed implant described in [52] (Fig. S5). Four components of the implant originally developed for chronic Neuropixels silicon probe recordings were used here: the two enclosures, the lid and the headstage lock. All parts were 3D printed with a resolution of 50 μm using a Form 2 3D printer (Formlabs, MA, United States) and Surgical Guide resin. After printing, the parts were cured with UV light for at least 15 minutes (Form cure, Formlabs), and then covered with copper tape from the inside to shield the implant from electrical noise. A 32-channel Intan headstage connected to the ZIF-to-Omnetics adapter PCB was fixed to the inner side of one of the enclosures using the headstage lock (Fig. S5A). Next, the probe was connected to the adapter, then the enclosure with the headstage was cemented to the skull using light-curable dental cement (RelyX Universal Resin Cement), followed by the fixation of the second enclosure. The copper shielding and the cable of the headstage were then connected to the ground/reference screw. After that, the lid was placed on top of the enclosures and secured in place using adhesive tape (Fig. S5B). Betadine (Mundipharma, Cambridge, England) was applied to the skin around the implant. Finally, the

Table 1

Summary statistics of acute rodent experiments. The numbers in parentheses indicate the number of recordings used for spike sorting and single unit analysis.

	No. of animals	No. of insertions	No. of recordings	No. of recordings with edge type probes	No. of recordings with center type probes	No. of edge type probes tested	No. of center type probes tested
Rats	9	13	26	16 (12)	10 (10)	3	3
Mice	3	5	9	5 (5)	4 (4)	1	1

rats were transferred to the animal facility. For at least five days, they received antibiotics (Augmentin, Glaxo Wellcome Production, Mayenne, France; 20 mg/kg body weight) and analgesics (Panadol Baby, Farmacclair, Hérouville-Saint-Clair, France; 2 mg/ml).

Recording sessions were performed in a dark, sound attenuating chamber (Med Associates; Fairfax, VT, United States). Throughout sessions, the animal could be easily and swiftly connected to and removed from the Intan recording system through the small rectangular aperture located on the lid of the implant structure, without the need to remove the lid from the top of the enclosures (e.g., see Fig. S5C). We recorded neural activity daily for about two weeks, starting on the day following probe implantation. Approximately 20–30 minutes of data were collected during each recording session, during which we also measured the electrical impedance of the implanted microelectrodes at 1 kHz.

2.4. Data analysis

2.4.1. Spike sorting and extraction of single unit quality metrics

To isolate the activity of single neurons, we applied spike sorting. A MATLAB-based software, Kilosort2 was used for automatic sorting with the default parameters [53]. Next, Phy2 (<https://github.com/kwikteam/phy>) was applied for manual curation of single unit clusters provided by Kilosort2. Clusters with atypical spike waveform shapes, and those exhibiting noise were excluded from further analysis. Additional criteria for excluding single unit clusters included a low firing rate (< 0.05 Hz, or fewer than 100 spikes) and a highly contaminated refractory period visible on the autocorrelogram (see examples of autocorrelograms of accepted single units in Fig. S4). Next, for each isolated single unit, we calculated the average multichannel spike waveform from the wideband recording (e.g., see Fig. 5B and D). We then computed the trough-to-peak amplitude of the mean spike waveforms. This spike amplitude was defined as the difference between the lowest point (trough) and the largest positive peak of the spike waveform (see inset in Fig. 6A), measured on the channel with the largest spike amplitude. In addition, we computed the signal-to-noise ratio (SNR) of all isolated single units using the quality metrics module of SpikeInterface [54]. To obtain the SNR, the maximum amplitude of the mean spike waveform of the single unit on the best channel is divided by the standard deviation of the background noise on the same channel estimated with the median absolute deviation.

2.4.2. Detection of up-state onsets and computation of up-state onset locked depth profiles

We used a multiunit activity (MUA)-based method to determine the onset of cortical up- and down-states (Fig. 8A), following the approach described in [38,45]. Briefly, we first extracted high frequency components from the wideband recordings using a third-order Butterworth bandpass filter (500–5000 Hz, zero-phase shift) and rectified the filtered signal. After that, we selected five cortical channels with robust MUA, then summed the samples across channels, resulting in a single-channel time series displaying the momentary intensity of cortical population activity. Next, the summed signal was smoothed with a third-order Butterworth lowpass filter (50 Hz, zero-phase shift). To determine the starting time of up- and down-states, we first computed an amplitude threshold level. For that, the average and standard deviation of cortical activity measured during down-states (i.e., lack of action potential firing) was calculated on the smoothed MUA signal. For state detection, we applied a threshold level which was the sum of the average and 2.5 times the standard deviation. Additional criteria were a minimum duration of 50 ms and 100 ms for up- and down-states, respectively. To compute local field potential (LFP, filtered between 0.1 – 500 Hz) and MUA (filtered between 500 – 5000 Hz and rectified) depth profiles (Fig. 8B and C), short snippets were extracted from the continuous, 24-channel recordings around the identified up-state onsets (100 ms before and 300 ms after the onset), then averaged across up-states. Nonfunctional/defective channels were not removed or interpolated in

these depth profiles. Additionally, we estimated the noise level in the frequency band between 500 and 5000 Hz from in vivo recordings (for $n = 49$ cortical electrodes of 3 probes). For each electrode, the RMS value was computed within a 50-ms-long window positioned at the center of down-states lasting at least 200 ms. These values were then averaged across down-states.

2.4.3. Current source density analysis

The one-dimensional kernel current source density (kCSD) method was used to estimate the density of transmembrane current sources from the recorded local field potentials [55,56]. The previously calculated up-state onset locked LFP depth profile (see Section 2.4.2) was used to compute the kCSD depth profile (Fig. 8D). The kCSD method is capable of estimating the CSD from arbitrary microelectrode configurations; hence, channels corresponding to nonfunctional microelectrodes ($n = 3$) were removed from the LFP depth profile before the kCSD calculation.

2.4.4. Sleep stage scoring in chronic recordings

To identify different stages of the sleep-wake cycle in naturally sleeping rats implanted with flexible probes [45], we first calculated spectrograms from LFP recordings using Chronux (v2.12) [57]. Spectrograms were computed in the range of 0.1–100 Hz on a channel located at the border of the neocortex and the hippocampus (Fig. 9C). Non-rapid eye movement (NREM) sleep was characterized by low theta (5.5 – 8 Hz) and high delta (1 – 4 Hz) power (i.e., low theta/delta ratio), while rapid eye movement (REM) sleep as well as wake states were marked by increased theta and a decreased delta power (i.e., high theta/delta ratio). Furthermore, REM and wake states could be discriminated based on a weaker theta rhythm and the frequent occurrence of movement artifacts observed during wakefulness.

2.5. Histological procedures

Nissl-staining was performed to identify the tracks of our polymer probes in brain tissue and to verify the recoding location, similarly as described in [38,58]. In brief, following both the acute and chronic experiments, animals were deeply anesthetized with a high dose of ketamine/xylazine. Then, to fixate the brain tissue, they were perfused through the heart, first with 100 ml of physiological saline solution which was followed by 250 ml of 4 % paraformaldehyde in 0.1 M phosphate buffer (pH = 7.4). Next, the fixed brain was removed from the skull, placed in the same fixative solution and kept at 4°C before further histological processing. Next, using a vibratome (Leica VT1200, Leica Microsystems, Wetzlar, Germany), we cut 60- μ m-thick coronal brain sections. These slices were then washed in 0.1 M phosphate buffer and moved to a gelatin-filled Petri dish. From the Petri dish, the brain slices were carefully placed on microscope slides, then were air dried. After that, cresyl violet (Nissl) staining was applied on the sections followed by dehydration in xylene. Slides were then covered with glass coverslips using DePex (SERVA Electrophoresis, Heidelberg, Germany). Finally, the Nissl-stained sections were photographed under an optical microscope (Leica DM2500, Leica Microsystems) fitted with a digital microscope camera (DP73, Olympus, Tokyo, Japan).

2.6. Statistical analysis

All data are presented as mean \pm standard deviation (SD). To determine whether the investigated metrics (e.g., spike amplitude, single unit yield) exhibit a normal distribution, we applied the Shapiro-Wilk test. For comparing two groups (e.g., edge type vs. center type probes), the two-tailed Student's *t*-test was applied for variables with a normal distribution, while the nonparametric Mann-Whitney *U* test was used for other variables. *P* values less than 0.05 were considered statistically significant. Boxplots illustrating the distribution of data are presented as follows (Figs. 3B, 6 and 7; Fig. S2C and D). The line in the middle of the box represents the median, whereas the edges of box mark

the 25th and 75th percentiles. Whiskers indicate the minimum and maximum values, while the black dot represents the average value. Smaller colored dots show individual values.

3. Results and discussion

We developed a 10- μm -thick polyimide-based laminar probe for invasive neural recordings comprising a 3.9-mm-long and 75–280- μm -wide, tapered shank and a 500- μm -wide flexible, spiral-shaped cable with a length of approximately 27 centimeters (Figs. 1 and 2). The probe shank accommodates 24 circular gold microelectrodes, each with a diameter of 20 μm and arranged linearly at a center-to-center distance of 150 μm . Two different shank layouts were designed and fabricated: edge type probes contain microelectrodes close to the edge of the polymer shank, while for center type probes, electrodes are centered on the shank (Figs. 1B and 2B). In addition, two alternative designs were realized for connecting the probes to the electrophysiological recording equipment: devices with a zero insertion force (ZIF) interface and probes with an interface for Omnetics connectors (Fig. 1C). For probes with a ZIF interface, a custom ZIF-to-Omnetics adapter PCB was used for connection to the recording system (Fig. 2C). All spiral probe variants were fabricated on 4-inch silicon wafers using standard thin-film micro-fabrication processes (Fig. 1D; refer to Section 2.2 for fabrication details).

To characterize our probes, we first measured the electrical impedance of several microelectrodes at frequencies relevant for neural recordings (0.1 – 7500 Hz), in vitro in saline solution (Fig. 3A). At 1 kHz, which corresponds to the short duration spikes of neurons, and thus, to single and multiunit activity, the impedance of microelectrodes was found to be $265.71 \pm 180.94 \text{ k}\Omega$ ($n = 265$ electrodes from a total of 360 electrodes on 15 probes), within the range adequate for low-noise, high-quality recordings of extracellular action potentials. To further reduce electrode impedance and consequently lower the noise level of neural recordings, PEDOT (Poly(3,4-ethylenedioxythiophene)) can be deposited onto the gold microelectrodes after fabrication [59–62]. About 26 % of the tested electrodes ($n = 95$) exhibited either very high or low impedance, indicating broken wires or shorts, respectively. These electrodes were considered as nonfunctional/defective. Consequently, the yield of functional electrodes was on average 76 % on each probe ($n =$

18 electrodes/probe). On the examined probes, we identified between 1 and 12 nonfunctional electrodes, with center type probes generally having more defective sites. The relatively low electrode yield can be attributed to two main factors. First, the spiral probes cover a relatively large area on the wafer. With an increased probe area, the likelihood of particle-originated defects increases, which may cause open circuits in the interconnection tracks. Second, the electroplating step used to reduce the line resistance of the interconnecting cables might cause shorts between adjacent tracks. It is important to note, however, that process optimization for improved fabrication yield was not targeted in this feasibility study. The track resistance of microelectrodes ($n = 15$) with a cable length of approximately 270 mm was found to be $756.40 \pm 123.91 \text{ }\Omega$, comparable to those reported in the literature for thin-film electrodes [63–65].

To assess the noise level in recordings obtained with our flexible probes, we performed in vitro measurements in saline solution. Noise in the local field potential (1–500 Hz) and the action potential (500 – 5000 Hz) bands were found to be $4.21 \pm 1.94 \text{ }\mu\text{V}_{\text{RMS}}$ and $2.24 \pm 0.45 \text{ }\mu\text{V}_{\text{RMS}}$, respectively ($n = 68$ electrodes of 3 probes; Fig. 3B). Furthermore, the noise level estimated in the action potential band from in vivo recordings (see Section 2.4.2 for details) was found to be $3.43 \pm 0.45 \text{ }\mu\text{V}_{\text{RMS}}$ ($n = 49$ cortical electrodes of 3 probes; Fig. 3B), slightly higher compared to noise measured in vitro recordings. The observed in vivo and in vitro noise levels closely match those reported for high-density silicon-based probes [44,66,67] and polymer-based devices [68].

Next, to test the recording capabilities of our devices in acute experiments, we implanted several probes into the brain tissue of anesthetized rats and mice. Details of these experiments are summarized in Table 1. Probes were implanted either with the aid of silicon dummy probes ($n = 3$ insertions; Fig. S1A) or with a 3D printed holder providing support during probe insertion ($n = 15$ insertions; Fig. S1B). In the latter case, the probe was temporarily attached to the holder with PEG. Dissolving the PEG and detaching the probe from the 3D printed holder did not degrade the quality of recordings (Fig. S2), although minor displacements ($< 150 \text{ }\mu\text{m}$) of the probe along the dorsoventral axis were occasionally observed (e.g., see Fig. S2A). Fig. 4 shows thalamocortical (slow) and hippocampal (gamma) oscillations, as well as spiking activity recorded with an edge type probe in a rat (Fig. 4A) and a mouse (Fig. 4B). The tested probes provided high-quality neural signals from both species, with high amplitude spikes visible on several channels. In the low frequency band (LFP; 0.1 – 500 Hz), we could observe the alternation of the two phases of the thalamocortical slow wave activity, a brain rhythm characteristic to ketamine/xylazine anesthesia with a frequency peak of around 1.5 Hz (see cortical channels in Fig. 4A and B; [38,69]). Furthermore, hippocampal gamma activity (30 – 60 Hz) was also frequently visible in the recordings (e.g., see hippocampal channels in Fig. 4A). The anatomical location of the microelectrodes could be reliably identified with post-mortem histology (Fig. 4C and D). It is worth noting that, without an insertion guide, the probes might slightly deviate (a few degrees) from the planned insertion trajectory due to their flexibility (Fig. 4C and D). The recording quality provided by center type probes was comparable to edge type probe data; however, the number of nonfunctional/noisy channels was generally higher for the tested center type probes (Fig. S3).

Investigating changes in the spiking activity of individual neurons recorded with implantable neural probes is a commonly applied method to address research questions in neuroscience. To assess the single unit recording capabilities of our probes, we performed spike sorting on the acquired acute rodent data, then determined the single unit yield and calculated the amplitude and signal-to-noise ratio of single unit spike waveforms. Fig. 5 displays short snippets of unit activity on channels containing high-amplitude spikes in the investigated brain structures (Fig. 5A), as well as multichannel spike waveforms and autocorrelograms of well-isolated single units (Fig. 5B, see more examples in Fig. S4). In the total of 31 acute recordings, we isolated 298 single units (9.61 ± 7.28 units/recording) with an average spike amplitude of 64.55

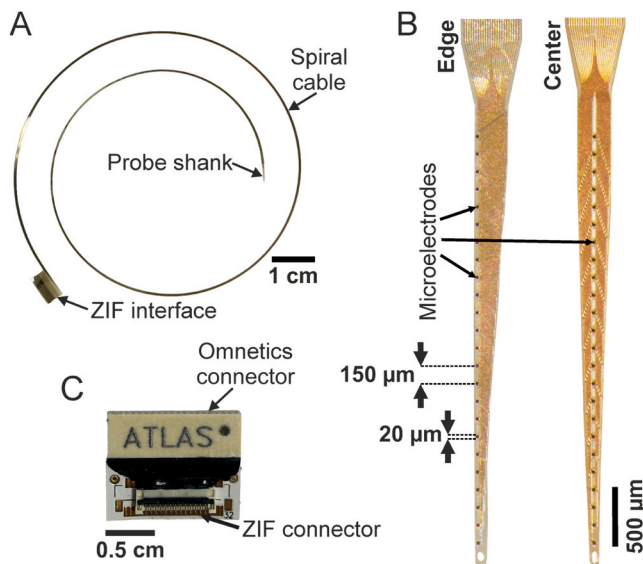


Fig. 2. Fabricated spiral probes. (A) Photograph of a spiral probe with zero insertion force (ZIF) interface released from the 4-inch silicon wafer. (B) Optical micrographs of the shank region of an edge type (left) and a center type (right) probe. (C) Photograph of a ZIF-to-Omnetics adapter printed circuit board used to connect the probe to the electrophysiological recording system.

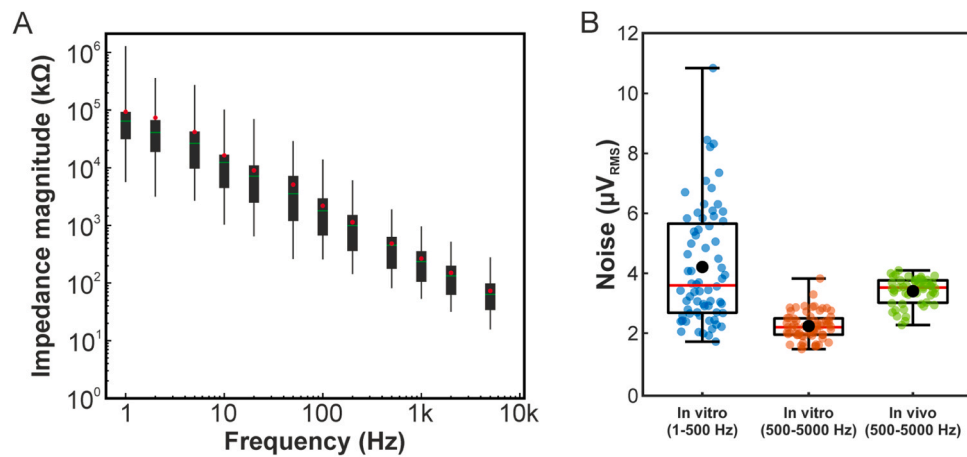


Fig. 3. In vitro characterization of flexible probes. (A) Electrical impedance magnitudes of microelectrodes ($n = 265$) measured in vitro at different frequencies (from 1 to 7500 Hz). Data are plotted on a logarithmic scale. Red dots represent the average values. (B) Distribution of the root mean square (RMS) noise of microelectrodes ($n = 68$ electrodes of 3 probes) measured in physiological saline solution in the frequency band corresponding to local field potentials (1–500 Hz, left) and unit activity (500 – 5000 Hz, middle). The RMS noise of electrodes ($n = 49$ cortical electrodes of 3 probes) in the action potential band was also estimated from in vivo cortical data obtained in anesthetized rats (right). The black dot represents the average value. Colored dots indicate individual noise values.

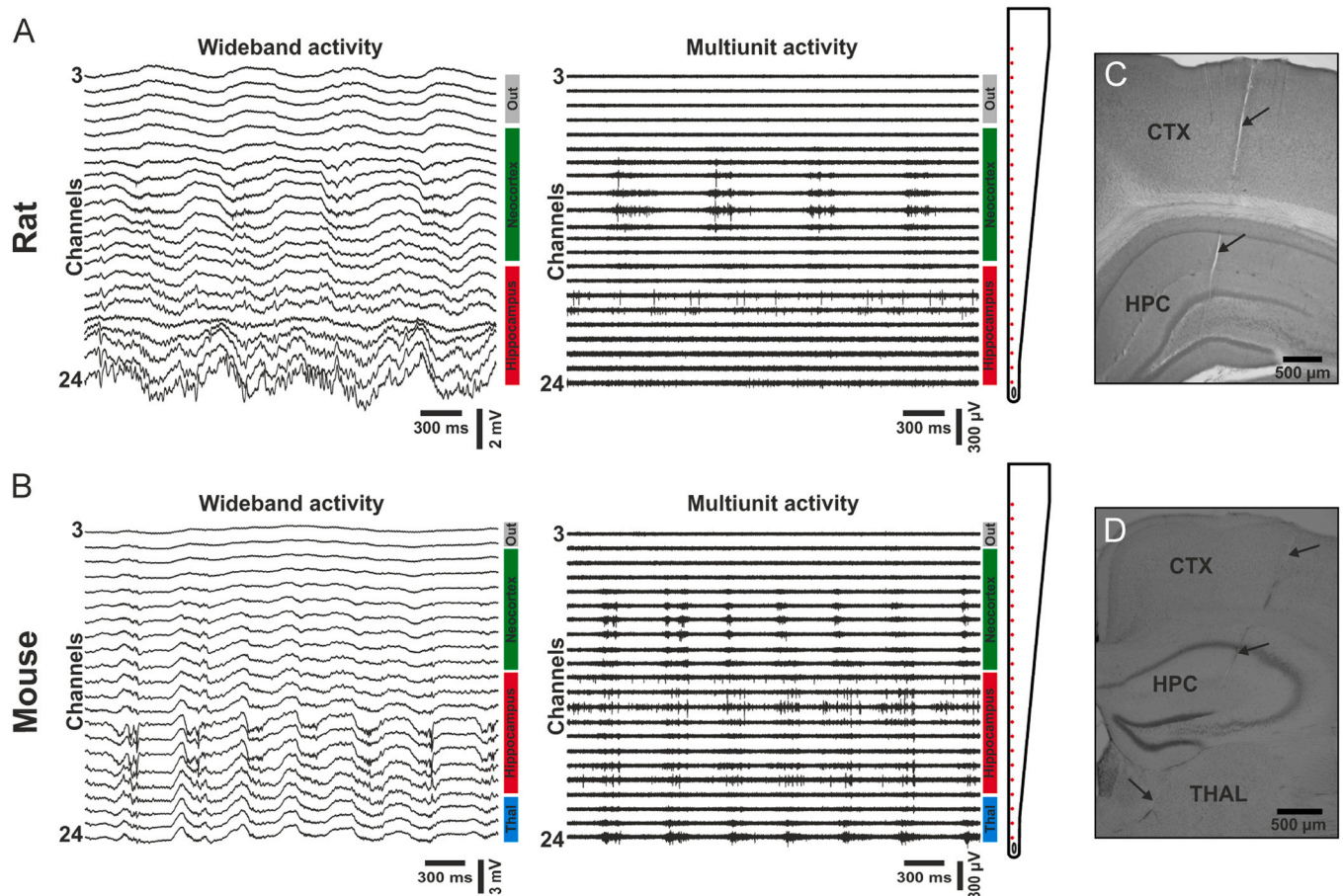


Fig. 4. Acute in vivo recordings from rodents. Representative three second long wideband (left; 0.1 – 7500 Hz) and multiunit activity (right; 500 – 5000 Hz) traces from the neocortex and hippocampus of a ketamine/xylazine anesthetized rat (A) and mouse (B). The first two channels (located outside the brain tissue) were removed due to noise and artefact contamination. Edge type probes were used for both recordings (see the schematic of the probe shank on the right side of the panels). The approximate anatomical location of microelectrodes is indicated with colored vertical bars next to the traces. Nissl-stained coronal brain sections of a rat (C) and a mouse (D) showing the probe track (black arrows) in the neocortex, hippocampus and thalamus (the latter only for the mouse). CTX, neocortex; HPC, hippocampus; Thal/THAL, thalamus; Out, outside the brain tissue.

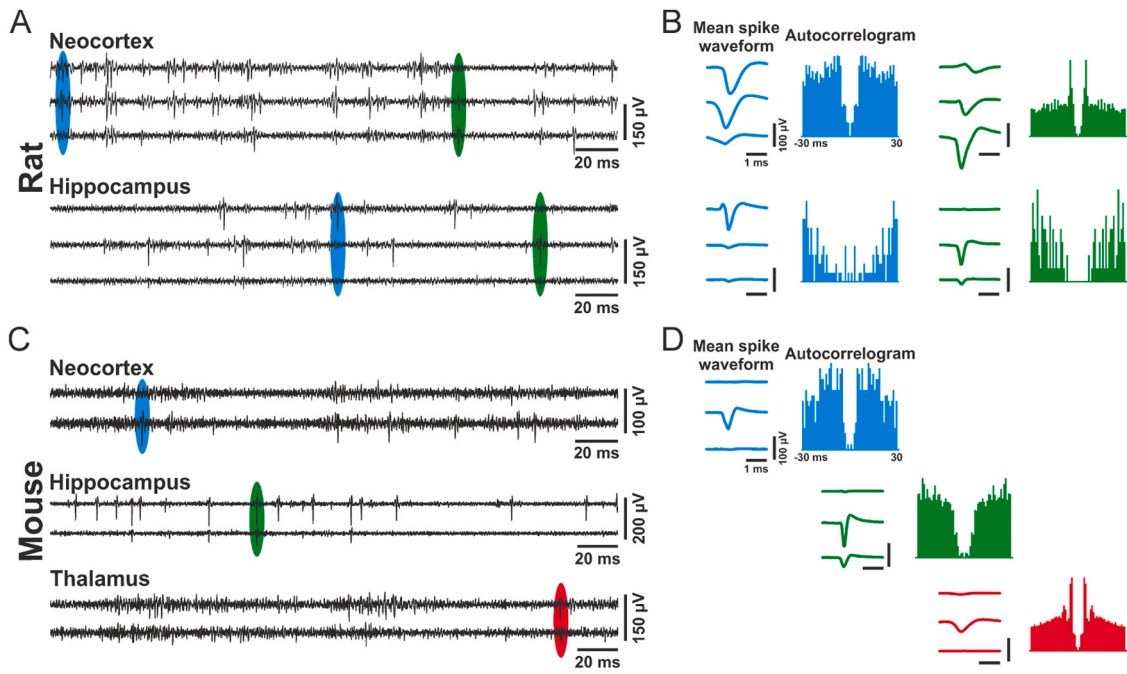


Fig. 5. Single unit activity in acute in vivo recordings. (A) Cortical (top) and hippocampal (bottom) unit activity traces (500 – 5000 Hz) from a rat displaying high amplitude single units. For each region, the traces were recorded by adjacent microelectrodes. (B) Average wideband multichannel action potential waveforms and autocorrelograms of two single units from each brain region shown in panel A. A single spike of each neuron is indicated in panel A with a colored ellipse. (C) Cortical (top), hippocampal (middle) and thalamic (bottom) unit activity traces (500 – 5000 Hz) from a mouse displaying high amplitude single units. (D) Average wideband multichannel action potential waveforms and autocorrelograms of an example single unit from each brain region displayed in panel C. A single spike of each neuron is indicated in panels C with a colored ellipse. The three channels showing the average spike waveforms represent data from adjacent microelectrodes.

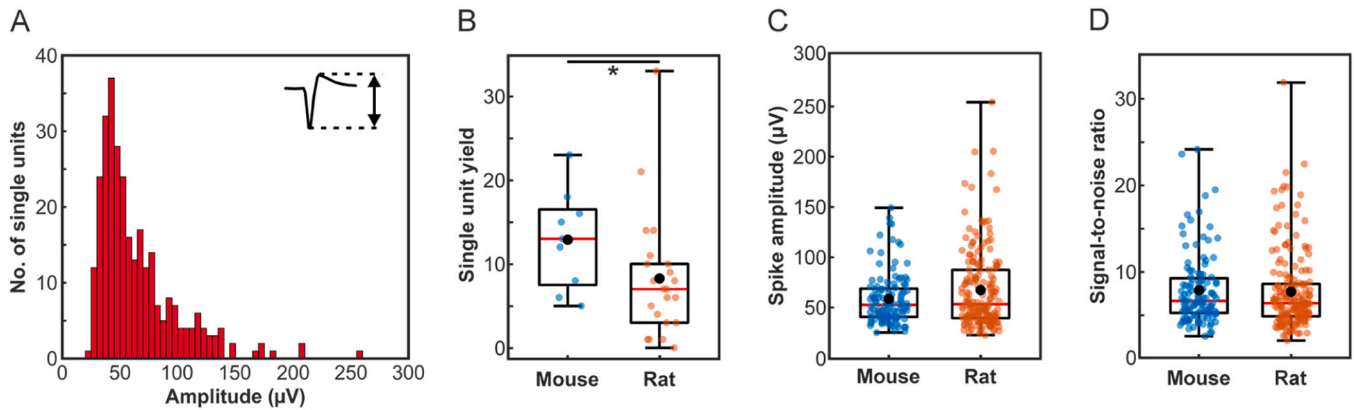


Fig. 6. Yield and quality metrics of single units. (A) Distribution of trough-to-peak amplitudes of the mean spike waveforms (see inset) of single units isolated from all acute rat and mouse recordings ($n = 298$ units). Single unit yield (B), trough-to-peak spike amplitudes (C) and signal-to-noise ratio (D) of single units isolated in mouse (left; $n = 116$ units) and rat (right; $n = 182$ units) recordings. The black dot represents the average value. Colored dots indicate values of individual recordings, spike amplitudes and single unit signal-to-noise ratios (blue and orange for mouse and rat recordings, respectively). * $p < 0.05$.

$\pm 34.73 \mu\text{V}$ (range: $23.27 - 255.05 \mu\text{V}$; Fig. 6A). Interestingly, significantly more single units could be separated in mouse recordings compared to recordings from rats (12.89 ± 5.88 units/recording vs. 8.27 ± 7.49 units/recording, respectively; $p = 0.041$; Mann Whitney U test; Fig. 6B). Although the spike amplitudes of these neurons were slightly lower in mice ($59.03 \pm 25.64 \mu\text{V}$ in mice vs. $68.06 \pm 39.10 \mu\text{V}$ in rats; Fig. 6C), the difference was not significant. The signal-to-noise ratio of single units was similar between the two species (7.89 ± 4.10 in mice vs. 7.73 ± 4.50 in rats; Fig. 6D). The higher single unit yield found in mouse recordings might be partially attributed to the higher neuron density in mice compared to rats (e.g., $\sim 5.5 \times 10^4$ neurons/ mm^3 in rats vs. $\sim 9.2 \times 10^4$ neurons/ mm^3 in mice in the neocortex [70–72]).

Recent studies have indicated that, compared to microelectrodes

positioned in the center of the implanted shank of silicon probes, microelectrodes placed closer to the edge of the shank provide slightly better signal quality in the frequency range corresponding to extracellular action potentials [67,73]. To examine potential differences in single unit recording capabilities between our edge and center type polyimide probes, we compared the single unit yields and spike amplitudes obtained with these two probe types. Significantly more single units could be isolated in recordings acquired with edge type probes compared to center type probes (12.94 ± 7.55 units/recording vs. 5.57 ± 4.48 units/recording, respectively; $p = 0.003$; Student's t-test; Fig. 7A). However, the number of identified nonfunctional electrodes was notably higher in the case of center type probes (6.7 ± 3.1 electrodes vs. 3.2 ± 2.1 sites; center vs. edge). To correct for this bias, for

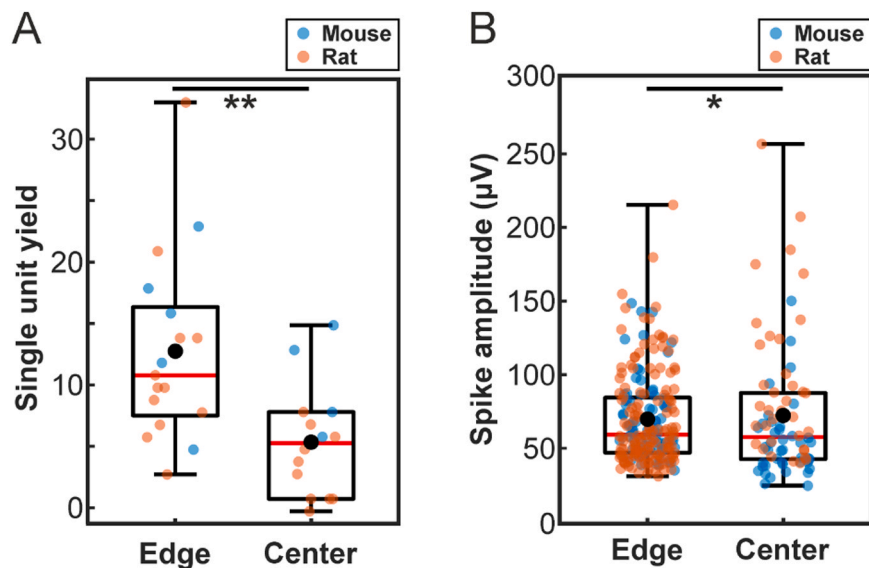


Fig. 7. Recording performance of edge and center type probes. Single unit yield (A) and trough-to-peak spike amplitudes of single units (B) isolated from recordings obtained with edge type (left; $n = 220$ units) and center type (right; $n = 78$ units) microelectrode configurations. The black dot represents the average value. Colored dots indicate values of individual recordings and spike amplitudes (blue and orange for mouse and rat recordings, respectively). * $p < 0.05$; ** $p < 0.01$.

each recording, we calculated the number of isolated single units per single electrode by dividing the total number of units by the number of functional electrodes. The results remained significantly different ($p = 0.010$; Student's *t*-test), with a higher number of units recorded with edge probes (0.61 ± 0.35 units/electrode vs. 0.31 ± 0.24 units/electrode; edge vs. center). The difference in single unit yields is in agreement with the findings of Seymour and colleagues [74]. In their study, edge sites on custom-designed parylene-based probes recorded more than twice as many units than sites located further from the edge of the shank. Interestingly, however, the spike amplitude of neurons recorded with our center type probes was slightly higher compared to probes with edge electrodes (72.70 ± 43.70 μV vs 61.66 ± 30.52 μV , respectively; $p = 0.049$; Mann Whitney U test; Fig. 7B), which is in contrast to what was found in [74]. We hypothesize that the higher number of defective and noisy channels found on center type probes may have slightly biased the spike sorting process, making the algorithm less likely to detect lower amplitude but still good quality single units.

Neural probes with equidistantly placed linear microelectrode arrays are well-suited for the precise spatial localization of transmembrane current sources and neuronal activity in laminar brain structures such as the neocortex or the hippocampus [36–38,75]. In rats, using laminar silicon probe recordings, we recently characterized the depth profiles of spontaneously occurring cortical slow waves induced with ketamine/xylazine anesthesia [38]. Here, we aimed to replicate these depth profiles using data recorded with our flexible polymer probes. First, we identified the onsets of active and silent states alternating during slow wave activity (i.e., up- and down-states), similar to the approach as described in Fiath et al. ([38]; Fig. 8A). Next, we calculated the LFP and multiunit activity (MUA) depth profiles locked to the onset of detected cortical up-states (Fig. 8B and C). The results for both LFP and MUA depth profiles were comparable to those computed from silicon probe recordings. During up-states, a positive potential deflection was apparent close to the cortical surface, accompanied by negative potentials in deeper layers, and with a polarity reversal in superficial layers

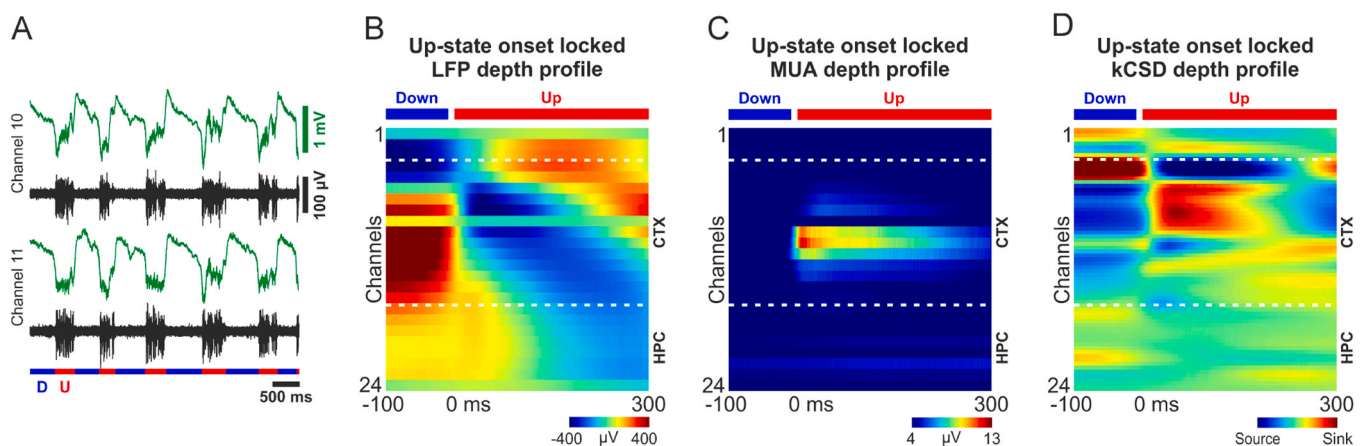


Fig. 8. Up-state locked laminar depth profiles computed from an acute rat recording. (A) Two adjacent cortical channels (green, wideband; black, multiunit activity) showing the alternation of up- and down-states emerging during ketamine/xylazine anesthesia in the thalamocortical system. The colored horizontal bars indicate the detected states (down-state, D, blue; up-state, U, red). (B) Local field potential (LFP; 0.1 – 500 Hz), (C) multiunit activity (MUA; 500 – 5000 Hz) and (D) kernel current source density (kCSD) depth profiles locked to the onset of detected up-states ($n = 7009$). The up-state starts at time point zero. The approximate border between the brain surface and the neocortex (CTX), as well as between the neocortex and hippocampus (HPC) are indicated with white horizontal dashed lines. The example recording contained three nonfunctional channels (channels 1, 9 and 24) which were not removed from the depth profiles shown in panels B and C.

(Fig. 8B). Conversely, during down-states, the LFP depth profile in the cortex exhibited the opposite pattern compared to up-states. Furthermore, spiking activity during up-states was the strongest in deep cortical layers, specifically in layer 5. The amplitude of the MUA decreased over time and as a function of distance from layer 5. As expected, no neuronal activity was observed during down-states (Fig. 8C). Finally, we estimated the current source density from the LFP using the kernel current source density method (kCSD; [55]; Fig. 8D). We observed a similar pattern of current sources and sinks in the computed kCSD depth profile as found in silicon probe recordings [38]. Namely, during up-states, two current sources (outward current) could be distinguished, a stronger source with a longer duration located close to the cortical surface, and a weaker and shorter source in deep layers (Fig. 8D; blue). At the same time, a broad and strong current sink (inward current) was present in the middle of the cortex (Fig. 8D; red). During down-states, the kCSD pattern reversed, with a strong and prolonged sink found at the top of the cortex and a strong current source with a larger extent located in the middle cortical layers (Fig. 8D). Although the 150 μm electrode pitch of this device is ideal for laminar recordings in the human neocortex [76], a smaller pitch might be more optimal for the rodent brain. Additionally, a higher electrode density would also improve the isolation of single units.

To assess the long-term functionality of the developed probes, we chronically implanted three devices in rats for a two-week period (Fig. S5). Wideband neural activity, as well as the impedance of microelectrodes at 1 kHz was measured every one or two days. The level of line (50 Hz) noise in recordings obtained with the spiral probes in freely moving rats was minimal and could be completely eliminated by using a Faraday cage (Fig. S6). The implanted probes successfully recorded both LFPs and spiking activity for several days across multiple channels (e.g., see Fig. 9A). Probes recorded activity from both the neocortex and the hippocampus (Fig. 9B), allowing us to differentiate various stages of the sleep-wake cycle during natural sleep in one of the rats (Fig. 9C). The LFP exhibited distinct patterns during different sleep stages, with prominent hippocampal theta activity during REM sleep and high-

amplitude cortical slow waves during NREM sleep (Fig. 9C, insets). In the case of the rat implanted with an edge type probe, the single unit yield during the first few days was comparable to that observed in acute recordings but gradually declined over time (Fig. 10A; Rat 1). The average spike amplitude of isolated neurons ranged between 60 and 100 μV throughout the experiment (Fig. 10B). Concurrently, the impedance values of functional microelectrodes gradually increased over time, starting from ~ 500 k Ω and reaching ~ 1500 k Ω (Fig. 10C). For the second rat, implanted with a center type probe, the number of separable single units rapidly declined after probe implantation, with the spike amplitudes of these neurons being also lower compared to the first rat (Fig. 10 A and B; Rat 2). The impedance of electrodes remained relatively stable, at approximately 500 k Ω over the two-week period (Fig. 10C). For the third rat, where a center type probe was implanted into the thalamus with a shuttle device, the unit yield was high after implantation, but single unit numbers were lower the next days (Fig. 10A). However, some low amplitude spikes could be detected even after two weeks. Interestingly, the impedance of functional electrodes decreased to about 100 k Ω within four days, then remained stable until the end of the investigated time period.

The results of chronic experiments suggest that the developed device is capable of recording neuronal activity for several days, though its performance starts to deteriorate the day after implantation. We attribute the decline in chronic signal quality to three main factors. First, despite the lower Young's modulus of polyimide compared to silicon, the designed dimensions of the implanted shank still result in a relative stiffness compared to the brain tissue. Consequently, similar to silicon probes, micromotions of the implanted device could potentially damage nearby neurons, enhance the foreign body response, and accelerate glial scar formation [14]. Second, the cross-sectional area of the probe shank is still relatively large. Combined with micromotions, this can further contribute to early neuronal death in the tissue surrounding the microelectrodes. Reducing the surgical footprint of the probe shank may mitigate both of these issues. Third, we observed a notable drop in the

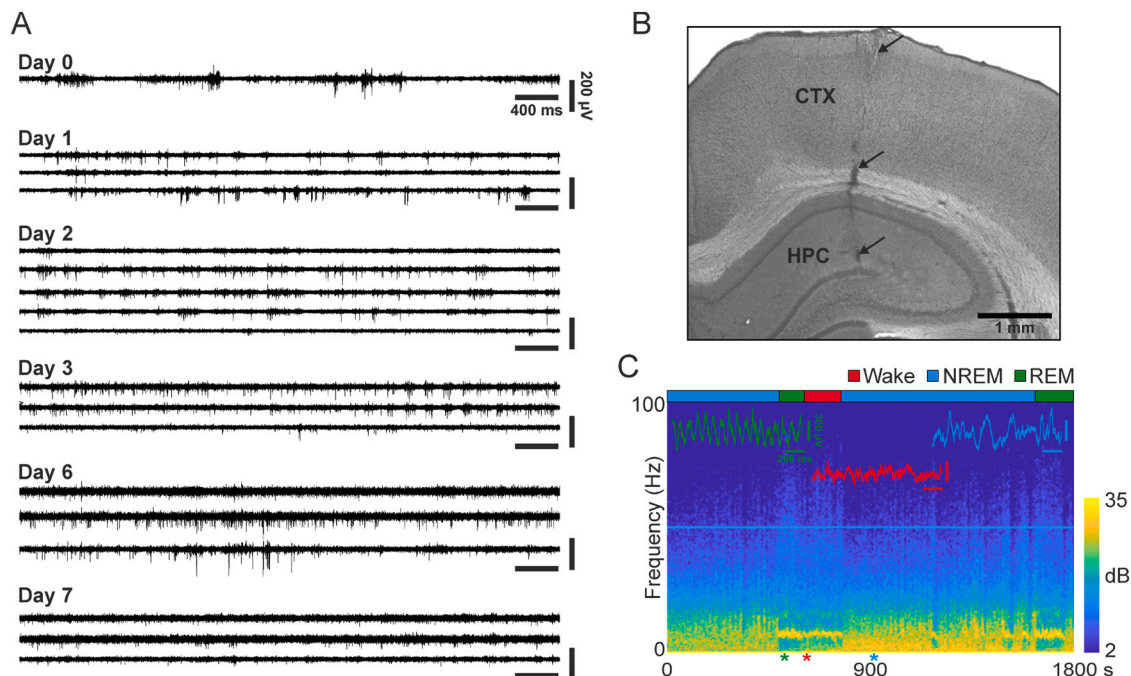


Fig. 9. Chronic in vivo recordings from a rat implanted with an edge type probe. (A) Unit activity (500 – 5000 Hz) on different channels recorded during different days in a chronically implanted rat. The probe was implanted on day 0. (B) Nissl-stained coronal brain section with the probe track (black arrows). CTX, neocortex; HPC, hippocampus. (C) Spectrogram of a 30-minute-long recording obtained one day after probe implantation showing different stages of the sleep-wake cycle (colored horizontal bars at the top of the spectrogram). Insets illustrate a color-coded two-second-long sample trace for each sleep stage. The time points corresponding to these traces are indicated with color-coded asterisks at the bottom of the spectrogram. Non-rapid eye movement sleep, NREM; rapid eye movement sleep, REM.

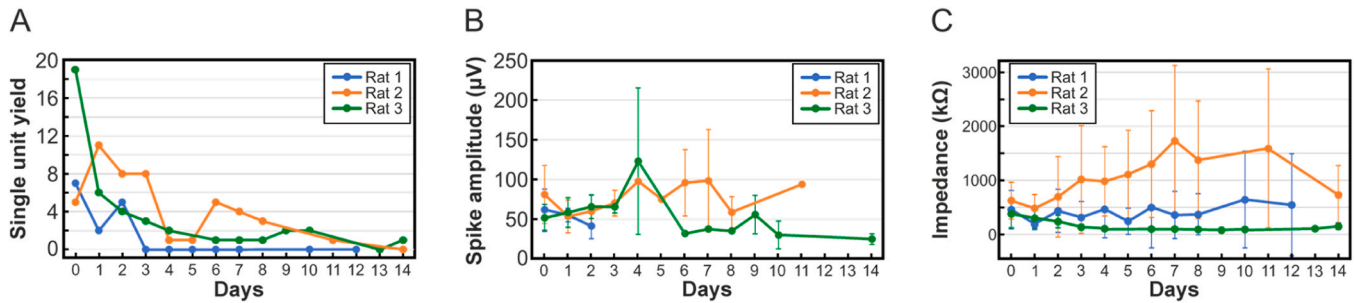


Fig. 10. Long-term recording performance of spiral probes. Changes in the single unit yield (A), trough-to-peak amplitude of mean single unit spike waveforms (B) and impedance magnitudes measured at 1 kHz (C) over the two-week recording period in chronically implanted rats. An edge type probe was implanted in Rat 1, while a center type probe was implanted in Rat 2 and Rat 3.

electrical impedance in some probes after a few days (e.g., see Rat 3 in Fig. 10C), suggesting potential issues with the insulating polyimide layers. Failure of insulation may result in fluid penetration into the probe shank, causing shorts, which in turn can significantly decrease the spike amplitudes of single units. In this study, our primary focus was on assessing the feasibility of the spiral design rather than fine-tuning the fabrication steps to enhance probe durability, but future developments should address this aspect. Furthermore, coating gold microelectrodes with PEDOT can reduce noise in neural recordings [59–62], potentially increasing the unit yield in chronic recordings by also allowing the isolation of single units with lower spike amplitudes.

4. Conclusions

We have demonstrated the design, fabrication and in vivo validation of a flexible polyimide-based penetrating neural probe featuring an exceptionally long extension cable (~27 cm), comparable in length to the cabling of clinical SEEG and deep brain electrodes. In this work, we realized two linear microelectrode configurations, namely edge and center designs, on a 10-μm-thick and ~4-mm-long tapered probe shank. The use of standard MEMS microfabrication technology, however, allows to fine-tune the geometrical properties and dimensions of the device, thus to manufacture other custom probe designs. For instance, an array of closely spaced microelectrodes placed on a longer shank can be designed for high-density neural recordings from deep brain structures of large animal species [77], or macroelectrodes can be positioned between microelectrodes for electrical stimulation purposes.

The microelectrodes located on the implantable probe shank were characterized using electrical impedance spectroscopy, revealing that over 70 % of the electrodes were functional. These electrodes displayed a low noise level and had an impedance of about 266 kΩ at 1 kHz in saline solution, suitable to provide high-fidelity neural recordings. Acute and chronic in vivo tests in the neocortex and hippocampus of rodents demonstrated that the proposed polymer probe can record high-quality local field potentials, as well as single and multiunit activities, even for several days. On average, around ten single units could be isolated from a single brain location, with an average spike amplitude of ~65 μV and a signal-to-noise ratio of approximately 7.8. The single unit yield was significantly higher for probes with microelectrodes located close to the edge of the shank compared to center type probes; however, spikes collected with the latter had slightly larger amplitudes. Furthermore, to demonstrate the potential applications of the probe, we applied the device to examine the laminar distribution of cortical slow wave activity and to identify different stages of the sleep-wake cycle in chronically implanted, naturally sleeping rats.

The developed flexible probe has a surgical footprint several magnitudes smaller compared to clinical electrodes typically used for the diagnosis and treatment of various brain disorders. This suggests the potential to reduce probe-related neuronal damage and foreign body response in the brain tissue by using these smaller devices. However, to

translate this technology for human clinical applications, or to use it in large animal models for basic research, a minimally invasive, accurate and efficient insertion method still needs to be developed. Furthermore, the long flexible cable designed for this device opens several potential application options. For example, in both small and large animal models, the extended cabling of the probe would allow for the placement of both the connector and the neural interface electronics (e.g., a neuro-stimulator, or a wireless transmitter for neural recording) away from the cranial window and the brain tissue, and, with adequately miniaturized equipment, implanted under the skin. This would result in a totally implantable device, similar to the pulse generator in patients with DBS electrodes where the device is implanted under the skin of the chest below the collarbone. This approach may reduce the risks of infections and complications associated with conventional chronic animal experiments, where an open wound is present in the skin around the recording/stimulating equipment on the head of the animal until the end of the experiment. In addition, placing the bulky equipment on the back (above or under the skin) would presumably impose fewer restrictions on the movement and daily life of the animal compared to when it is fixed on the skull.

CRedit authorship contribution statement

Csaba Horváth: Writing – original draft, Methodology, Investigation, Formal analysis, Data curation. **Klaudia Csikós:** Writing – original draft, Visualization, Resources, Methodology, Investigation. **Borbála Árkossy:** Visualization, Investigation, Formal analysis, Data curation. **Eric Klein:** Writing – original draft, Visualization, Methodology, Investigation. **Patrick Ruther:** Writing – review & editing, Writing – original draft, Visualization, Supervision, Resources, Methodology, Funding acquisition, Conceptualization. **István Ulbert:** Writing – review & editing, Writing – original draft, Supervision, Funding acquisition, Conceptualization. **Richard Fiath:** Writing – review & editing, Writing – original draft, Visualization, Supervision, Software, Project administration, Methodology, Investigation, Formal analysis, Data curation.

Declaration of Competing Interest

The authors declare no competing interests.

Data availability

Data will be made available on request.

Acknowledgements

The research leading to these results has received funding from the Hungarian Brain Research Program Grant (NAP2022-I-2/2022), the Pharmaceutical Research and Development Laboratory Project

(PharmaLab, RRF-2.3.1-21-2022-00015) and the New National Excellence Program of the Ministry for Culture and Innovation from the source of the National Research, Development and Innovation Fund (ÚNKP-23-5-PPKE-128 to R.F. and ÚNKP-22-1-I-PPKE-59 to B.Á.). This work is part of BrainLinks-BrainTools which is funded by the Federal Ministry of Economics, Science and Arts of Baden-Württemberg within the sustainability program for projects of the excellence initiative II (P. R.). R.F. was supported by the Bolyai János Scholarship of the Hungarian Academy of Sciences.

Appendix A. Supporting information

Supplementary data associated with this article can be found in the online version at [doi:10.1016/j.snb.2024.136220](https://doi.org/10.1016/j.snb.2024.136220).

References

- [1] H.Y. Chen, Y. Fang, Recent developments in implantable neural probe technologies, *Mrs Bull.* 48 (2023) 484–494, <https://doi.org/10.1557/s43577-023-00535-2>.
- [2] J.K. Krauss, N. Lipsman, T. Aziz, A. Boutet, P. Brown, J.W. Chang, B. Davidson, W. M. Grill, M.I. Hariz, A. Horn, M. Schulder, A. Mammis, P.A. Tass, J. Volkmann, A. M. Lozano, Technology of deep brain stimulation: current status and future directions, *Nat. Rev. Neurol.* 17 (2021) 75–87, <https://doi.org/10.1038/s41582-020-00426-z>.
- [3] A.C. Paulk, P. Salami, R. Zemann, S.S. Cash, Electrode development for epilepsy diagnosis and treatment, *Neurosurg. Clin. N. Am.* 35 (2024) 135–149, <https://doi.org/10.1016/j.neuc.2023.09.003>.
- [4] K. Iida, H. Otsubo, Stereoelectroencephalography: indication and efficacy, *Neurol. Med. Chir. (Tokyo)* 57 (2017) 375–385, <https://doi.org/10.2176/nmc.ra.2017-0008>.
- [5] Z. Fekete, Recent advances in silicon-based neural microelectrodes and microsystems: a review, *Sens. Actuatur B-Chem.* 215 (2015) 300–315, <https://doi.org/10.1016/j.snb.2015.03.055>.
- [6] P. Ruther, O. Paul, New approaches for CMOS-based devices for large-scale neural recording, *Curr. Opin. Neurobiol.* 32 (2015) 31–37, <https://doi.org/10.1016/j.conb.2014.10.007>.
- [7] B.C. Raducanu, R.F. Yazicioglu, C.M. Lopez, M. Ballini, J. Putzeys, S.W. Wang, A. Andrei, V. Rochus, M. Welkenhuysen, N. van Helleputte, S. Musa, R. Pueris, F. Kloosterman, C. Van Hoof, R. Fiath, I. Ulbert, S. Mitra, Time multiplexed active neural probe with 1356 parallel recording sites, *Sensors* 17 (2017) 2388, <https://doi.org/10.3390/s17102388>.
- [8] J.J. Jun, N.A. Steinmetz, J.H. Siegle, D.J. Denman, M. Bauza, B. Barbarits, A.K. Lee, C.A. Anastassiou, A. Andrei, C. Aydin, M. Barbic, T.J. Blanche, V. Bonin, J. Couto, B. Dutta, S.L. Gratiy, D.A. Gutnisky, M. Hausser, B. Karsh, P. Ledochowitsch, C. M. Lopez, C. Mitelut, S. Musa, M. Okun, M. Pachitariu, J. Putzeys, P.D. Rich, C. Rossant, W.L. Sun, K. Svoboda, M. Carandini, K.D. Harris, C. Koch, J. O'Keefe, T. D. Harris, Fully integrated silicon probes for high-density recording of neural activity, *Nature* 551 (2017) 232–236, <https://doi.org/10.1038/nature24636>.
- [9] N.A. Steinmetz, C. Aydin, A. Lebedeva, M. Okun, M. Pachitariu, M. Bauza, M. Beau, J. Bhagat, C. Bohm, M. Broux, S. Chen, J. Colonell, R.J. Gardner, B. Karsh, F. Kloosterman, D. Kostadinov, C. Mora-Lopez, J. O'Callaghan, J. Park, J. Putzeys, B. Sauerbrei, R.J.J. van Daal, A.Z. Vollan, S. Wang, M. Welkenhuysen, Z. Ye, J. T. Dudman, B. Dutta, A.W. Hantman, K.D. Harris, A.K. Lee, E.I. Moser, J. O'Keefe, A. Renart, K. Svoboda, M. Hausser, S. Haesler, M. Carandini, T.D. Harris, Neuropixels 2.0: A miniaturized high-density probe for stable, long-term brain recordings, *Science* 372 (2021) eabf4588, <https://doi.org/10.1126/science.abf4588>.
- [10] V.S. Polikov, P.A. Tresco, W.M. Reichert, Response of brain tissue to chronically implanted neural electrodes, *J. Neurosci. Methods* 148 (2005) 1–18, <https://doi.org/10.1016/j.jneumeth.2005.08.015>.
- [11] P.J. Rousche, R.A. Normann, Chronic recording capability of the Utah Intracortical Electrode Array in cat sensory cortex, *J. Neurosci. Methods* 82 (1998) 1–15, [https://doi.org/10.1016/S0165-0270\(98\)00031-4](https://doi.org/10.1016/S0165-0270(98)00031-4).
- [12] D.R. Kipke, R.J. Vetter, J.C. Williams, J.F. Hetke, Silicon-substrate intracortical microelectrode arrays for long-term recording of neuronal spike activity in cerebral cortex, *IEEE T Neur Sys Res* 11 (2003) 151–155, <https://doi.org/10.1109/Tnsre.2003.814443>.
- [13] J.R. Capadona, D.J. Tyler, C.A. Zorman, S.J. Rowan, C. Weder, Mechanically adaptive nanocomposites for neural interfacing, *Mrs Bull.* 37 (2012) 581–589, <https://doi.org/10.1557/mrs.2012.97>.
- [14] A. Gilletti, J. Muthuswamy, Brain micromotion around implants in the rodent somatosensory cortex, *J. Neural Eng.* 3 (2006) 189–195, <https://doi.org/10.1088/1741-2560/3/3/001>.
- [15] G.C. McConnell, H.D. Rees, A.I. Levey, C.A. Gutekunst, R.E. Gross, R. V. Bellamkonda, Implanted neural electrodes cause chronic, local inflammation that is correlated with local neurodegeneration, *J. Neural Eng.* 6 (2009) 056003, <https://doi.org/10.1088/1741-2560/6/5/056003>.
- [16] K.A. Potter, A.C. Buck, W.K. Self, J.R. Capadona, Stab injury and device implantation within the brain results in inversely multiphasic neuroinflammatory and neurodegenerative responses, *J. Neural Eng.* 9 (2012) 046020, <https://doi.org/10.1088/1741-2560/9/4/046020>.
- [17] R. Biran, D.C. Martin, P.A. Tresco, Neuronal cell loss accompanies the brain tissue response to chronically implanted silicon microelectrode arrays, *Exp. Neurol.* 195 (2005) 115–126, <https://doi.org/10.1016/j.expneurol.2005.04.020>.
- [18] B.D. Winslow, P.A. Tresco, Quantitative analysis of the tissue response to chronically implanted microwire electrodes in rat cortex, *Biomaterials* 31 (2010) 1558–1567, <https://doi.org/10.1016/j.biomaterials.2009.11.049>.
- [19] J.P. Seymour, D.R. Kipke, Neural probe design for reduced tissue encapsulation in CNS, *Biomaterials* 28 (2007) 3594–3607, <https://doi.org/10.1016/j.biomaterials.2007.03.024>.
- [20] X. Tang, H. Shen, S. Zhao, N. Li, J. Liu, Flexible brain–computer interfaces, *Nat. Electron.* 6 (2023) 109–118, <https://doi.org/10.1038/s41928-022-00913-9>.
- [21] J.W. Jeong, G. Shin, S.I. Park, K.J. Yu, L. Xu, J.A. Rogers, Soft materials in neuroengineering for hard problems in neuroscience, *Neuron* 86 (2015) 175–186, <https://doi.org/10.1016/j.neuron.2014.12.035>.
- [22] H. Wunderlich, K.L. Kozielski, Next generation material interfaces for neural engineering, *Curr. Opin. Biotechnol.* 72 (2021) 29–38, <https://doi.org/10.1016/j.copbio.2021.09.005>.
- [23] E. McGlynn, V. Nabaei, E. Ren, G. Galeote-Checa, R. Das, G. Curia, H. Heidari, The future of neuroscience: flexible and wireless implantable neural electronics, *Adv. Sci.* 8 (2021) 2002693, <https://doi.org/10.1002/adv.202002693>.
- [24] Y. Yang, K. Xu, S. Guan, J. Ding, J. Wang, Y. Fang, H. Tian, Ultraflexible neural probes for multidirectional neuronal activity recordings over large spatial and temporal scales, *Nano Lett.* 23 (2023) 8568–8575, <https://doi.org/10.1021/acs.nanolett.3c02348>.
- [25] K.C. Cheung, P. Renaud, H. Tanila, K. Djupsund, Flexible polyimide microelectrode array for in vivo recordings and current source density analysis, *Biosens. Bioelectron.* 22 (2007) 1783–1790, <https://doi.org/10.1016/j.bios.2006.08.035>.
- [26] L. Luan, X.L. Wei, Z.T. Zhao, J.J. Siegel, O. Potnis, C.A. Tuppen, S.Q. Lin, S. Kazmi, R.A. Fowler, S. Holloway, A.K. Dunn, R.A. Chitwood, C. Xie, Ultraflexible nanoelectronic probes form reliable, glial scar-free neural integration, *Sci. Adv.* 3 (2017) e1601966, <https://doi.org/10.1126/sciadv.1601966>.
- [27] S. Guan, H. Tian, Y. Yang, M. Liu, J. Ding, J. Wang, Y. Fang, Self-assembled ultraflexible probes for long-term neural recordings and neuromodulation, *Nat. Protoc.* 18 (2023) 1712–1744, <https://doi.org/10.1038/s41596-023-00824-9>.
- [28] X. Yang, T. Zhou, T.J. Zwang, G. Hong, Y. Zhao, R.D. Viveros, T.M. Fu, T. Gao, C. M. Lieber, Bioinspired neuron-like electronics, *Nat. Mater.* 18 (2019) 510–517, <https://doi.org/10.1038/s41563-019-0292-9>.
- [29] J. Liu, T.M. Fu, Z. Cheng, G. Hong, T. Zhou, L. Jin, M. Duvvuri, Z. Jiang, P. Kruskal, C. Xie, Z. Suo, Y. Fang, C.M. Lieber, Syringe-injectable electronics, *Nat. Nanotechnol.* 10 (2015) 629–636, <https://doi.org/10.1038/nnano.2015.115>.
- [30] Z. Zhao, H. Zhu, X. Li, L. Sun, F. He, J.E. Chung, D.F. Liu, L. Frank, L. Luan, C. Xie, Ultraflexible electrode arrays for months-long high-density electrophysiological mapping of thousands of neurons in rodents, *Nat. Biomed. Eng.* 7 (2023) 520–532, <https://doi.org/10.1038/s41551-022-00941-y>.
- [31] S. Zhao, X. Tang, W. Tian, S. Partarrieu, R. Liu, H. Shen, J. Lee, S. Guo, Z. Lin, J. Liu, Tracking neural activity from the same cells during the entire adult life of mice, *Nat. Neurosci.* 26 (2023) 696–710, <https://doi.org/10.1038/s41593-023-01267-x>.
- [32] J.K. Nguyen, D.J. Park, J.L. Skousen, A.E. Hess-Dunning, D.J. Tyler, S.J. Rowan, C. Weder, J.R. Capadona, Mechanically-compliant intracortical implants reduce the neuroinflammatory response, *J. Neural Eng.* 11 (2014) 056014, <https://doi.org/10.1088/1741-2560/11/5/056014>.
- [33] F. He, R. Lycke, M. Ganji, C. Xie, L. Luan, Ultraflexible neural electrodes for long-lasting intracortical recording, *iScience* 23 (2020) 101387, <https://doi.org/10.1016/j.isci.2020.101387>.
- [34] C. Bohler, M. Vomero, M. Soula, M. Voroslakos, M. Porto Cruz, R. Liljemalm, G. Buzsaki, T. Stieglitz, M. Asplund, Multilayer arrays for neurotechnology applications (MANTA): chronically stable thin-film intracortical implants, *Adv. Sci.* 10 (2023) e2207576, <https://doi.org/10.1002/adv.202207576>.
- [35] T. Zhou, G. Hong, T.M. Fu, X. Yang, T.G. Schuhmann, R.D. Viveros, C.M. Lieber, Syringe-injectable mesh electronics integrate seamlessly with minimal chronic immune response in the brain, *Proc. Natl. Acad. Sci. USA* 114 (2017) 5894–5899, <https://doi.org/10.1073/pnas.1705509114>.
- [36] R. Cserscsa, B. Dombóvari, D. Fábó, L. Wittner, L. Eross, L. Entz, A. Solyom, G. Rasonyi, A. Szucs, A. Kelemen, R. Jakus, V. Juhos, L. Grand, A. Magony, P. Halasz, T.F. Freund, Z. Maglóczy, S.S. Cash, L. Papp, G. Karmos, E. Halgren, I. Ulbert, Laminar analysis of slow wave activity in humans, *Brain* 133 (2010) 2814–2829, <https://doi.org/10.1093/brain/awq169>.
- [37] G. Buzsaki, J. Czopf, I. Kondakor, L. Kelenyi, Laminar distribution of hippocampal rhythmic slow activity (Rsa) in the behaving rat - current source density analysis, effects of urethane and atropine, *Brain Res.* 365 (1986) 125–137, [https://doi.org/10.1016/0006-8993\(86\)90729-8](https://doi.org/10.1016/0006-8993(86)90729-8).
- [38] R. Fiath, B.P. Kerekes, L. Wittner, K. Toth, P. Beregszaszi, D. Horvath, I. Ulbert, Laminar analysis of the slow wave activity in the somatosensory cortex of anesthetized rats, *Eur. J. Neurosci.* 44 (2016) 1935–1951, <https://doi.org/10.1111/ejn.13274>.
- [39] F. Barz, V. Trouillet, O. Paul, P. Ruther, CMOS-compatible, flexible, intracortical neural probes, *IEEE Trans. Biomed. Eng.* 67 (2020) 1366–1376, <https://doi.org/10.1109/TBME.2019.2936740>.
- [40] F. Pothof, L. Bonini, M. Lanzilotto, A. Livi, L. Fogassi, G.A. Orban, O. Paul, P. Ruther, Chronic neural probe for simultaneous recording of single-unit, multi-unit, and local field potential activity from multiple brain sites, *J. Neural Eng.* 13 (2016) 046006, <https://doi.org/10.1088/1741-2560/13/4/046006>.

- [41] D. Keppeler, M. Schwaerzle, T. Harczos, L. Jablonski, A. Dieter, B. Wolf, S. Ayub, C. Vogl, C. Wrobel, G. Hoch, K. Abdellatif, M. Jeschke, V. Rankovic, O. Paul, P. Ruthner, T. Moser, Multichannel optogenetic stimulation of the auditory pathway using microfabricated LED cochlear implants in rodents, *Sci. Transl. Med* 12 (2020), <https://doi.org/10.1126/scitranslmed.abb8086>.
- [42] M. Vomero, F. Ciarpella, E. Zucchini, M. Kirsch, L. Fadiga, T. Stieglitz, M. Asplund, On the longevity of flexible neural interfaces: establishing biostability of polyimide-based intracortical implants, *Biomaterials* 281 (2022) 121372, <https://doi.org/10.1016/j.biomaterials.2022.121372>.
- [43] E. Klein, C. Gossler, O. Paul, P. Ruthner, High-density μ LED-based optical cochlear implant with improved thermomechanical behavior, *Front Neurosci.* 12 (2018) 659, <https://doi.org/10.3389/fnins.2018.00659>.
- [44] R. Fiath, B.C. Raducanu, S. Musa, A. Andrei, C.M. Lopez, C. van Hoof, P. Ruthner, A. Aarts, D. Horvath, I. Ulbert, A silicon-based neural probe with densely-packed low-impedance titanium nitride microelectrodes for ultrahigh-resolution in vivo recordings, *Biosens. Bioelectron.* 106 (2018) 86–92, <https://doi.org/10.1016/j.bios.2018.01.060>.
- [45] C. Horváth, I. Ulbert, R. Fiath, Propagating population activity patterns during spontaneous slow waves in the thalamus of rodents, *Neuroimage* 285 (2024) 120484, <https://doi.org/10.1016/j.neuroimage.2023.120484>.
- [46] G. Paxinos, K.B.J. Franklin, *The mouse brain in stereotaxic coordinates*, Compact, second ed., Elsevier Academic Press, 2004.
- [47] G. Paxinos, C. Watson, *The Rat Brain in Stereotaxic Coordinates*, sixth ed., Elsevier Academic Press, 2007.
- [48] L. Grand, P. Anita, E. Vázsonyi, M. Gergely, D. Gubán, R. Fiath, B.P. Kerekes, K. György, U. István, B. Gábor, A novel multisite silicon probe for high quality laminar neural recordings, *Sens. Actuat A-Phys.* 166 (2011) 14–21, <https://doi.org/10.1016/j.sna.2010.12.019>.
- [49] K. Sharma, C. Boehler, M. Asplund, O. Paul, P. Ruthner, New wafer-level fabrication of ultrathin silicon insertion shuttles for flexible neural implants. 2023 IEEE 36th International Conference on Micro Electro Mechanical Systems (MEMS), Munich, Germany, 2023, pp. 421–424, <https://doi.org/10.1109/Mems49605.2023.10052581>.
- [50] S.H. Felix, K.G. Shah, V.M. Tolosa, H.J. Sheth, A.C. Tooker, T.L. Delima, S. P. Jadhav, L.M. Frank, S.S. Pannu, Insertion of flexible neural probes using rigid stiffeners attached with biodegradable adhesive, *J. Vis. Exp.* (2013) e50609, <https://doi.org/10.3791/50609>.
- [51] K.B. Bjugstad, K. Lampe, D.S. Kern, M. Mahoney, Biocompatibility of poly(ethylene glycol)-based hydrogels in the brain: an analysis of the glial response across space and time, *J. Biomed. Mater. Res A* 95 (2010) 79–91, <https://doi.org/10.1002/jbm.a.32809>.
- [52] A. Ghestem, M.N. Pompili, M. Dipper-Wawra, P.P. Quilichini, C. Bernard, M. Ferraris, Long-term near-continuous recording with NeuroPixels probes in healthy and epileptic rats, *J. Neural Eng.* 20 (2023) 046003, <https://doi.org/10.1088/1741-2552/ace218>.
- [53] M. Pachitariu, S. Sridhar, C. Stringer, Solving the spike sorting problem with Kilosort, *bioRxiv*, (2023), <https://doi.org/10.1101/2023.01.07.523036>.
- [54] A.P. Buccino, C.L. Hurwitz, S. Garcia, J. Magland, J.H. Siegle, R. Hurwitz, M. H. Hennig, SpikeInterface, a unified framework for spike sorting, *Elife* 9 (2020) e61834, <https://doi.org/10.7554/eLife.61834>.
- [55] J. Potworowski, W. Jakuczun, S. Leski, D. Wojcik, Kernel current source density method, *Neural Comput.* 24 (2012) 541–575, https://doi.org/10.1162/NECO_a_00236.
- [56] K.H. Pettersen, A. Devor, I. Ulbert, A.M. Dale, G.T. Einevoll, Current-source density estimation based on inversion of electrostatic forward solution: effects of finite extent of neuronal activity and conductivity discontinuities, *J. Neurosci. Methods* 154 (2006) 116–133, <https://doi.org/10.1016/j.jneumeth.2005.12.005>.
- [57] H. Bokil, P. Andrews, J.E. Kulkarni, S. Mehta, P.P. Mitra, Chronux: a platform for analyzing neural signals, *J. Neurosci. Methods* 192 (2010) 146–151, <https://doi.org/10.1016/j.jneumeth.2010.06.020>.
- [58] R. Fiath, A.L. Marton, F. Matyas, D. Pinke, G. Marton, K. Toth, I. Ulbert, Slow insertion of silicon probes improves the quality of acute neuronal recordings, *Sci. Rep.* 9 (2019) 111, <https://doi.org/10.1038/s41598-018-36816-z>.
- [59] X.Y. Cui, D.C. Martin, Electrochemical deposition and characterization of poly(3,4-ethylenedioxythiophene) on neural microelectrode arrays, *Sens. Actuat B-Chem.* 89 (2003) 92–102, [https://doi.org/10.1016/S0925-4005\(02\)00448-3](https://doi.org/10.1016/S0925-4005(02)00448-3).
- [60] K.A. Ludwig, N.B. Langhals, M.D. Joseph, S.M. Richardson-Burns, J.L. Hendricks, D.R. Kipke, Poly(3,4-ethylenedioxythiophene) (PEDOT) polymer coatings facilitate smaller neural recording electrodes, *J. Neural Eng.* 8 (2011) 014001, <https://doi.org/10.1088/1741-2560/8/1/014001>.
- [61] A.S. Pranti, A. Schander, A. Bödecker, W. Lang, PEDOT: PSS coating on gold microelectrodes with excellent stability and high charge injection capacity for chronic neural interfaces, *Sens. Actuat B-Chem.* 275 (2018) 382–393, <https://doi.org/10.1016/j.snb.2018.08.007>.
- [62] C.M. Lewis, C. Boehler, R. Liljefalm, P. Fries, T. Stieglitz, M. Asplund, Recording quality is systematically related to electrode impedance, *Adv. Healthc. Mater.* (2024) e2303401, <https://doi.org/10.1002/adhm.202303401>.
- [63] D. Farina, K. Yoshida, T. Stieglitz, K.P. Koch, Multichannel thin-film electrode for intramuscular electromyographic recordings, *J. Appl. Physiol.* 104 (2008) 821–827, <https://doi.org/10.1152/japplphysiol.00788.2007>.
- [64] G. Schiavone, F. Fallegger, K. Kang, B. Barra, N. Vachicouras, E. Roussinova, I. Furfaro, S. Jiguet, I. Seanez, S. Borgognon, A. Rowald, Q. Li, C. Qin, E. Bezaud, J. Bloch, G. Courtine, M. Capogrosso, S.P. Lacour, Soft, implantable bioelectronic interfaces for translational research, *Adv. Mater.* 32 (2020) e1906512, <https://doi.org/10.1002/adma.201906512>.
- [65] G. Schiavone, N. Vachicouras, Y. Vyza, S.P. Lacour, Dimensional scaling of thin-film stimulation electrode systems in translational research, *J. Neural Eng.* 18 (2021) 046054, <https://doi.org/10.1088/1741-2552/abf607>.
- [66] J.J. Jun, N.A. Steinmetz, J.H. Siegle, D.J. Denman, M. Bauza, B. Barbarits, A.K. Lee, C.A. Anastassiou, A. Andrei, C. Aydin, M. Barbic, T.J. Blanche, V. Bonin, J. Couto, B. Dutta, S.L. Gratiy, D.A. Gutnisky, M. Hausser, B. Karsh, P. Ledochowitsch, C. M. Lopez, C. Mitelut, S. Musa, M. Okun, M. Pachitariu, J. Putzeys, P.D. Rich, C. Rossant, W.L. Sun, K. Svoboda, M. Carandini, K.D. Harris, C. Koch, J. O'Keefe, T. D. Harris, Fully integrated silicon probes for high-density recording of neural activity, *Nature* 551 (2017) 232–236, <https://doi.org/10.1038/nature24636>.
- [67] R. Fiath, D. Meszena, Z. Somogyvari, M. Boda, P. Bartho, P. Ruthner, I. Ulbert, Recording site placement on planar silicon-based probes affects signal quality in acute neuronal recordings, *Sci. Rep.* 11 (2021) 2028, <https://doi.org/10.1038/s41598-021-81127-5>.
- [68] R. Fiath, K.T. Hofer, V. Csikos, D. Horvath, T. Nanasi, K. Toth, F. Pothof, C. Bohler, M. Asplund, P. Ruthner, I. Ulbert, Long-term recording performance and biocompatibility of chronically implanted cylindrically-shaped, polymer-based neural interfaces, *Biomed. Tech. (Berl.)* 63 (2018) 301–315, <https://doi.org/10.1515/bmt-2017-0154>.
- [69] A.V. Sharma, T. Wolansky, C.T. Dickson, A comparison of sleep-like slow oscillations in the hippocampus under ketamine and urethane anesthesia, *J. Neurophysiol.* 104 (2010) 932–939, <https://doi.org/10.1152/jn.01065.2009>.
- [70] S. Herculano-Houzel, B. Mota, R. Lent, Cellular scaling rules for rodent brains, *Proc. Natl. Acad. Sci. USA* 103 (2006) 12138–12143, <https://doi.org/10.1073/pnas.0604911103>.
- [71] A. Schuz, G. Palm, Density of neurons and synapses in the cerebral-cortex of the mouse, *J. Comp. Neurol.* 286 (1989) 442–455, <https://doi.org/10.1002/cne.902860404>.
- [72] J.Q. Ren, Y. Aika, C.W. Heizmann, T. Kosaka, Quantitative-analysis of neurons and glial-cells in the rat somatosensory cortex, with special reference to gabaergic neurons and parvalbumin-containing neurons, *Exp. Brain Res.* 92 (1992) 1–14, <https://doi.org/10.1007/BF00230378>.
- [73] H.C. Lee, J. Gaire, B. Roysam, K.J. Otto, Placing sites on the edge of planar silicon microelectrodes enhances chronic recording functionality, *IEEE T Bio-Med Eng.* 65 (2018) 1245–1255, <https://doi.org/10.1109/Tbme.2017.2715811>.
- [74] J.P. Seymour, N.B. Langhals, D.J. Anderson, D.R. Kipke, Novel multi-sided, microelectrode arrays for implantable neural applications, *Biomed. Micro* 13 (2011) 441–451, <https://doi.org/10.1007/s10544-011-9512-z>.
- [75] U. Mitzdorf, Current source-density method and application in cat cerebral-cortex - investigation of evoked-potentials and eeg phenomena, *Physiol. Rev.* 65 (1985) 37–100, <https://doi.org/10.1152/physrev.1985.65.1.37>.
- [76] I. Ulbert, E. Halgren, G. Heit, G. Karmos, Multiple microelectrode-recording system for human intracortical applications, *J. Neurosci. Methods* 106 (2001) 69–79, [https://doi.org/10.1016/S0165-0270\(01\)00330-2](https://doi.org/10.1016/S0165-0270(01)00330-2).
- [77] M. Keller, O. Paul, P. Ruthner, Highly Flexible, Ultra-long SEEG Probes with IrOx Micro Electrodes Realized using Compact Bond Interfaces, in *MNE 2023, 49th Int. Conf. on Micro- and Nano Engineering*, Berlin, Germany, 25–28. September 2023, (2023) 628–629.

Csaba Horváth received his MSc degree in Biology from the University of Szeged, Hungary, in 2019. He is currently pursuing a PhD degree at the Semmelweis University, János Szentágothai Doctoral School of Neurosciences, Budapest, Hungary. He is primarily engaged in the investigation of neural signals within the thalamocortical system using high-density neural probes.

Klaudia Csikós earned her BSc and MSc degrees from the Faculty of Information Technology at Pázmány Péter Catholic University, Budapest, Hungary, in 2021 and 2023, respectively. Currently, she is dedicated to her doctoral studies at the János Szentágothai Doctoral School of Neurosciences at Semmelweis University, Budapest, Hungary. Her current research interests include the development and validation of modular multimodal neural interfaces and functional ultrasound imaging in large animal models.

Borbála Árkossy obtained her BSc degree from the Faculty of Information Technology, Pázmány Péter Catholic University, Budapest, Hungary in 2023. She is continuing her studies in the Health Engineering MSc program at Budapest University of Technology and Economics, Hungary. Her research interests include neural implant and brain imaging technologies.

Eric Klein obtained his BSc and MSc degrees from the University of Freiburg. During his BSc, he focused on connector systems for clinical electrocorticography electrodes while in his MSc, he contributed to an early prototype of an optical cochlear implant. Joining the Microsystems Materials Lab at IMTEK in 2016, he has been actively involved in the development and optimization of optical cochlear implants. Having completed his PhD in 2023, he now serves as a postdoc, dedicating his efforts to the development of micro-light emitting diodes (μ LEDs) for a diverse range of optogenetic research applications.

Patrick Ruthner received his Diploma in physics and a PhD in mechanical engineering in 1993 and 1996, respectively. During his post-doctoral position at the Research Center Karlsruhe (1996–1998) he focused on LIGA-based microoptical components. Since 1998 he has been a Senior Scientist at the Department of Microsystems Engineering (IMTEK), University of Freiburg designing, fabricating, and characterizing CMOS-compatible MEMS devices, particularly those for biomedical applications such as neuroscience and optogenetics. He co-founded the spin-off company ATLAS Neuroengineering in Belgium and is a member of the Cluster of Excellence BrainLinks-BrainTools at the University of Freiburg.

István Ulbert obtained a degree in electrical engineering from the Budapest University of Technology, Hungary in 1988, and a general medical degree from Semmelweis University, Budapest, Hungary in 1997. In 2002, he obtained his PhD in neuroscience at the Doctoral School of Semmelweis University, Budapest, Hungary. Later he was awarded the title of Doctor of the Hungarian Academy of Sciences in 2014. He is currently the director of the Institute of Cognitive Neuroscience and Psychology of the HUN-REN Research Centre for Natural Sciences and a professor at Pázmány Péter Catholic University, Budapest, Hungary. He is the author of more than 130 journal articles, including many published in the most prestigious journals in the field of science, such as Science, Nature Neuroscience, Neuron, PNAS, Brain and The Journal of Neuroscience. His main area of interest is the

development of implantable bioelectronics and the investigation of intracortical generators of brain oscillations.

Richárd Fiáth received his MSc degree in electrical and computer engineering from the Faculty of Information Technology, Pázmány Péter Catholic University, Budapest, Hungary in 2009, and his PhD degree in neurosciences from the Semmelweis University, Budapest, in 2017. He is currently a senior research fellow at the Institute of Cognitive Neuroscience and Psychology, Research Centre for Natural Sciences, Budapest, Hungary. His main research interests include implantable neural interfaces, neurostimulation, thalamocortical oscillations and the physiology of sleep.